Appl. Phys. B 87, 503–521 (2007)
DOI: 10.1007/s00340-007-2619-5

Applied Physics B
Lasers and Optics

H.A. MICHELSEN[1,✉]
F. LIU[2]
B.F. KOCK[3]
H. BLADH[4]
A. BOIARCIUC[5]
M. CHARWATH[6]
T. DREIER[7]
R. HADEF[8]
M. HOFMANN[3]
J. REIMANN[9]
S. WILL[9]
P.-E. BENGTSSON[4]
H. BOCKHORN[6]
F. FOUCHER[5]
K.-P. GEIGLE[10]
C. MOUNAÏM-ROUSSELLE[5]
C. SCHULZ[3]
R. STIRN[10]
B. TRIBALET[3]
R. SUNTZ[6]

Modeling laser-induced incandescence of soot: a summary and comparison of LII models

[1] Combustion Research Facility, Sandia National Labs, Livermore, CA, USA
[2] National Research Council, Ottawa, Ontario, Canada
[3] IVG, Universität Duisburg-Essen, Duisburg, Germany
[4] Department of Combustion Physics, Lund Institute of Technology, Lund, Sweden
[5] Université d'Orléans, Orléans, France
[6] Universität Karlsruhe, Karlsruhe, Germany
[7] Paul Scherrer Institut, Villigen, Switzerland
[8] Institut de Génie Mécanique, Université Larbi Ben M'Hidi, Oum El Bouaghi, Algeria
[9] Technische Thermodynamik, Universität Bremen, Bremen, Germany
[10] Institute of Combustion Technology, DLR, Stuttgart, Germany

Received: 16 October 2006/Revised version: 19 January 2007
Published online: 25 April 2007 •

ABSTRACT We have performed a comparison of ten models that predict the temporal behavior of laser-induced incandescence (LII) of soot. In this paper we present a summary of the models and comparisons of calculated temperatures, diameters, signals, and energy-balance terms. The models were run assuming laser heating at 532 nm at fluences of 0.05 and 0.70 J/cm^2 with a laser temporal profile provided. Calculations were performed for a single primary particle with a diameter of 30 nm at an ambient temperature of 1800 K and a pressure of 1 bar. Preliminary calculations were performed with a fully constrained model. The comparison of unconstrained models demonstrates a wide spread in calculated LII signals. Many of the differences can be attributed to the values of a few important parameters, such as the refractive-index function $E(m)$ and thermal and mass accommodation coefficients. Constraining these parameters brings most of the models into much better agreement with each other, particularly for the low-fluence case. Agreement among models is not as good for the high-fluence case, even when selected parameters are constrained. The reason for greater variability in model results at high fluence appears to be related to solution approaches to mass and heat loss by sublimation.

PACS 65.80.+n; 78.20.Nv; 42.62.-b; 44.05.+e

1 Introduction

Laser-induced incandescence (LII) has become a popular technique for measurements of soot concentration and primary particle size. This technique has been implemented in a large number of applications under a wide range of conditions. LII involves heating particles with a high-power pulsed laser (usually with a pulse duration of several nanoseconds) and measuring the radiative emission from the hot particles. The magnitude of the signal depends on the particle volume fraction, making it a useful technique for measuring soot spatial and temporal distributions [1–13]. The signal decay rate depends on the specific surface area of the particles. At intermediate and high fluences the decay rate is very strongly influenced by volume loss from sublimation. The correlation between specific surface area and signal decay rate has been extensively exploited to infer primary particle size. Using such measurements for quantitative determinations of particle volume fraction and size requires a detailed understanding of experimental parameters and physical mechanisms that control the LII signal.

One approach to developing such a description of LII signal generation involves modeling the processes that control signal production. Considerable effort has been devoted to developing models capable of predicting LII signals in response to pulsed laser heating over a range of fluences [4, 10, 14–41]. Current models solve the energy- and mass-balance equations to predict the temporal response of the particle to pulsed laser heating. LII models typically account for particle heating by laser absorption and cooling by conduction to surrounding gases, sublimation of carbon clusters, and emission of thermal radiation. Some models have been optimized to fit LII signal decay curves for inferring primary particle sizes [19–31], whereas others have been used primarily to understand the influence of factors such as experimental parameters, particle characteristics, and physical processes that occur during particle heating and cooling [32–41].

Despite widespread use of LII for particle measurements and a large body of experimental and modeling work aimed at developing a firm understanding of the technique, there

✉ Fax: +1-925-294-2276, E-mail: hamiche@sandia.gov

are severe limitations in the fundamental understanding of LII signal generation and significant uncertainties in measurement interpretations, which were highlighted in a recent LII workshop [42, 43]. In this paper we compare the results of ten models in order to assess the state of our understanding of the mechanisms involved and the uncertainties in the analysis of LII data. This comparison is meant to resolve questions raised by a previous model comparison performed during the first LII workshop, which was held in Duisburg, Germany in September 2005 [43]. An example set of results from the Duisburg meeting is shown in Fig. 1. The calculated signals spanned so many orders of magnitude that they could not be compared without normalization. At low fluence, calculated signal decay rates varied wildly (Fig. 1a). At high fluence both the rise times and decay times demonstrated large variability (Fig. 1b). Identifying the reasons for such variability was extremely difficult, and the most significant conclusion of this exercise was the startling realization that the models used by different groups yielded such different predictions despite using the same model conditions and nominally similar calculation approaches.

The comparison presented in this paper is a product of the second LII workshop, which took place in Bad Herrenalb, Germany in August 2006 [44] and was aimed at resolving some of the questions introduced at the first workshop [42, 43]. The results of the model comparison presented in Duisburg demonstrated the importance of performing a more systematic comparison of available models. In this paper we compare model results for a limited set of conditions. Calculations were performed for a single excitation wavelength (532 nm) at two laser fluences (0.05 and 0.70 J/cm^2) for a single primary particle 30 nm in diameter at an ambient pressure of 1 bar and a typical flame temperature of 1800 K. Using these conditions allowed us to focus on fundamental differences between models while avoiding complications from factors such as low ambient temperatures, high ambient pressures, and particle aggregate morphology and size. We have also summarized the methodologies and parameters used in the LII models included in this comparison and used this information to identify sources of differences between model results. This paper does not intend to provide recommendations for the best model approaches or parameters for the prediction of LII signals.

We first compare results from a fully constrained model in which all groups ran calculations using the same set of equations and input parameters. This test demonstrates the consistency in the way in which parameters are input into the models and signals are calculated. Using the same laser input, ambient conditions, and assumptions about particle size and detection conditions, each group also performed unconstrained model calculations with a model they currently use for LII data analysis. These comparisons demonstrate considerable variability among the independent models but much better agreement (i.e. within the same order of magnitude) than shown by the previous comparisons (Fig. 1). In order to determine whether the main source of the variability observed in the present comparison was from differences in values of important input parameters or from inherent differences in the physical model formulations, each group ran their LII model with a subset of constrained parameters with the same input conditions used in the calculations described above. The results of this set of calculations indicate that much (although not all) of the variability at low fluence is attributable to the range of values used for a few important parameters. At high fluence, however, differences in the treatment of heat and mass loss by sublimation lead to significant differences between models.

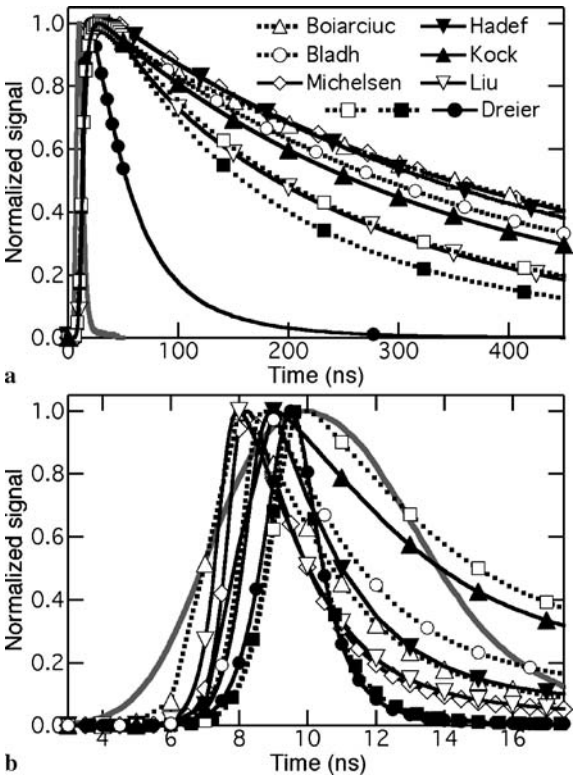

FIGURE 1 Comparison of modeled LII temporal profiles. These results are from the first international LII workshop [42, 43]. The models shown have been described previously [42]. Calculations were performed for an ambient temperature of 1800 K and a pressure of 1 bar, an excitation wavelength of 532 nm, a single primary particle with a diameter of 30 nm, and laser fluences of (**a**) 0.05 J/cm^2 and (**b**) 0.70 J/cm^2. Model results were scaled to 1 at the maximum. The laser temporal profile is represented by the *solid gray curve*

2 Methodology

In order to establish the consistency of model input and calculated signal output procedures, a set of model cases was run using a fully constrained model described in Sect. 2.1. Participants were given values of input parameters and equations for heating, cooling, and mass-loss rates. The laser temporal profile (shown in Fig. 2) was provided in numerical format. Calculations were performed for a laser wavelength of 532 nm, an ambient temperature of 1800 K, an ambient pressure of 1 bar, and a primary particle size of 30 nm at laser fluences of 0.05 J/cm^2 and 0.70 J/cm^2 for a homogeneous laser spatial profile. The signal was calculated at a wavelength of 500 nm for a single primary particle integrated over the entire particle surface assuming an infinitely fast detector.

In a second set of calculations, each group ran the model they currently use for LII data analysis. These calculations were based on the same laser temporal profile, wavelength,

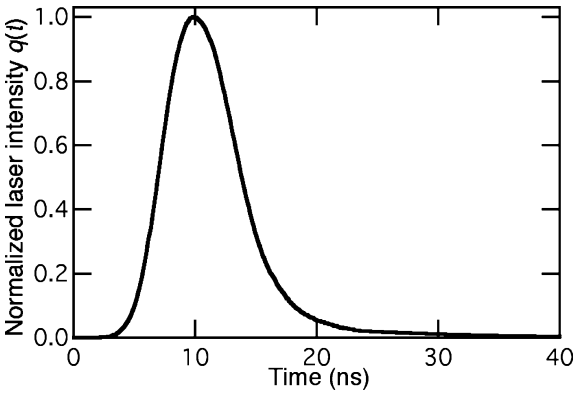

FIGURE 2 Laser temporal profile used in the models. The profile was scaled to 1 at the peak

and fluences, ambient temperature and pressure, particle size, and emission wavelength as specified for the fully constrained model runs. In these model runs equations and parameters (other than those applying to input/output conditions) were not specified. Section 2.2 summarizes the independent unconstrained models.

In a third set of calculations, each group ran their independent model with a subset of constrained parameters. These calculations were similarly performed with the same laser profile, wavelength, and fluences, ambient conditions, particle size, and output conditions used in the other sets of calculations.

2.1 *Description of the fully constrained model*

The fully constrained model used in the comparison is based on the Melton model [16], in which the energy- and mass-balance equations are solved as a set of coupled differential equations for changes in particle temperature and size in response to pulsed laser heating. The energy-balance equation is expressed as

$$\frac{\mathrm{d}U_{\mathrm{Internal}}}{\mathrm{d}t} = \dot{Q}_{\mathrm{Absorption}} - \dot{Q}_{\mathrm{Sublimation}} - \dot{Q}_{\mathrm{Conduction}}\,, \tag{1}$$

where each of the terms represents a rate of energy loss or gain. The equation is a function of time t, temperature T, mass M, and primary particle diameter D.

2.1.1 Internal energy. The rate of change of the energy stored by the particle is given by

$$\frac{\mathrm{d}U_{\mathrm{Internal}}}{\mathrm{d}t} = \varrho_{\mathrm{s}} c_{\mathrm{s}} \frac{\pi}{6} D^3 \frac{\mathrm{d}T}{\mathrm{d}t}\,, \tag{2}$$

where ϱ_{s} and c_{s} are the density and specific heat of soot. Values of ϱ_{s} and c_{s} are given in Table 1.

2.1.2 Absorption. In the original Melton work [16], the particle laser energy absorption rate was calculated using an unpublished computer code that solved the Mie equations for a spherical particle. Under the conditions investigated here ($D \ll \lambda_1$), the Rayleigh approximation can be used to calculate the absorption rate according to

$$\dot{Q}_{\mathrm{Absorption}} = \frac{\pi^2 D^3 E(m)}{\lambda_1} \frac{F q(t)}{q_1}\,, \tag{3}$$

where F is the fluence, $q(t)$ is the laser temporal profile normalized to 1 at the peak for this comparison, q_1 is a constant that normalizes the integrated laser temporal profile to unity, λ_1 is the laser wavelength, and $E(m)$ is a function of the complex refractive index. For the purposes of this study, using (3) to calculate $\dot{Q}_{\mathrm{Absorption}}$ is more convenient and instructive than solving the full Mie equations. Table 2 gives the values

Model	c_{s} (J/g K)	ϱ_{s} (g/cm^3)
Melton (original) [16]	1.90	2.26
Melton (workshop)	1.90	2.26
Semi-constrained	1.90	2.26
Bladh	T-dependent[a]	$2.3031–7.3106 \times 10^{-5} T$ [36]
Boiarciuc	2.1	1.9 [39]
Charwath	1.9 [51]	1.86 [51]
Dreier	T-dependent[b]	1.86 [56]
Hadef	T-dependent[a]	$2.3031–7.3106 \times 10^{-5} T$ [36]
Hofmann	T-dependent[b]	1.86 [56]
Kock	T-dependent[b]	1.86 [56]
Liu	T-dependent[c]	1.9 [39]
Michelsen	T-dependent[a]	$2.3031–7.3106 \times 10^{-5}$ T [36]
Will	T-dependent[d]	1.85 [57]

[a] $c_{\mathrm{s}} = \left(\frac{R}{12.01\ \mathrm{g/mol}}\right)\left\{1.115\left(\frac{597\ \mathrm{K}}{T}\right)^2 \exp\left(\frac{597\ \mathrm{K}}{T}\right)\left[\exp\left(\frac{597\ \mathrm{K}}{T}\right)-1\right]^{-2} + 1.789\left(\frac{1739\ \mathrm{K}}{T}\right)^2 \exp\left(\frac{1739\ \mathrm{K}}{T}\right)\left[\exp\left(\frac{1739\ \mathrm{K}}{T}\right)-1\right]^{-2} + \frac{T}{8620\ \mathrm{K}}\right\}$ [36, 47]

[b] $c_{\mathrm{s}} = 1.878\ \mathrm{J/g\,K} + 1.082 \times 10^{-4}\ \mathrm{J/g\,K^2}\,T - \frac{1.5149 \times 10^5\ \mathrm{J\,K/g}}{T^2}$ [30]

[c] $c_{\mathrm{s}}(0–1200\ \mathrm{K}) = -9.7768 \times 10^{-4} + 2.7943 \times 10^{-4} T + 1.4554 \times 10^{-5} T^2 - 3.4432 \times 10^{-8} T^3 + 3.6700 \times 10^{-11} T^4 - 1.9485 \times 10^{-14} T^5 + 4.1802 \times 10^{-18} T^6$
$c_{\mathrm{s}}(1200–5500\ \mathrm{K}) = 2.9497 \times 10^{-1} + 2.9614 \times 10^{-3} T - 2.1232 \times 10^{-6} T^2 + 8.1901 \times 10^{-10} T^3 - 1.7516 \times 10^{-13} T^4 + 1.9628 \times 10^{-17} T^5 - 8.9817 \times 10^{-22} T^6$

[d] $c_{\mathrm{s}} = 2.90041\ \mathrm{J/g\,K} - 36.4073\ \mathrm{J/g\,K^{0.5}} \frac{1}{\sqrt{T}}$ from a fit to NIST-JANAF data [46]

TABLE 1 Parameters for U_{Internal}

TABLE 2 Parameters for $\dot{Q}_{\text{Absorption}}$ and $\dot{Q}_{\text{Radiation}}$

Model	$E(m)$ at 500 and 532 nm	$E(m)$ broadband
Melton (original) [16]	0.18	$\lambda/4\pi D$
Melton (workshop)	0.23	Not applicable
Semi-constrained	0.23	0.23
Bladh	0.2165 [58]	0.2165 [58]
Boiarciuc	0.30	$0.232+\lambda(1.2546\times10^3\ \text{cm}^{-1})$[b]
Charwath	0.179 [58]	0.179 [58]
Dreier	0.24	0.24
Hadef	0.26 [59]	$(0.13\beta/\pi)(k_\text{B}T/hc)^{\xi-1}$ [c]
Hofmann	0.40	$\lambda/4\pi D$
Kock	0.23 [60]	$\lambda/4\pi D$
Liu	0.38	0.40 [38]
Michelsen	0.34[a]	0.32
Will	0.26 [59]	0.26 [59]

[a] Effective value for linear component of absorption
[b] Derived from analyses presented by Krishnan et al. [61] and fitted by Snelling et al. [38]
[c] Effective value for use in (8) [36]

of $E(m)$ used in this comparison and the value assumed in the original reference based on an index of refraction at 532 nm of $1.92-0.51\text{i}$ [16].

2.1.3 Sublimation. In the constrained model the evaporative-cooling rate is represented as

$$\dot{Q}_{\text{Sublimation}} = -\frac{\Delta H_\text{v}}{W_\text{s}}\frac{\text{d}M}{\text{d}t}\,, \tag{4}$$

where W_s is the molecular weight of solid (atomic) carbon and ΔH_v is the enthalpy of formation of sublimed carbon clusters. In this model only C_3 is assumed to sublime. There is some ambiguity in the original reference concerning the value of the molecular weight to be used in this equation because the subscript on W is missing in the $\dot{Q}_{\text{Sublimation}}$ term of the energy-balance equation [16]. Given that ΔH_v is associated with the sublimed clusters (C_3), the molecular weight used in (4) should probably be that of the sublimed clusters W_v. For the workshop comparison, however, we used the value associated with the solid phase for atomic carbon. The mass lost through sublimation is calculated according to

$$\frac{\text{d}M}{\text{d}t} = \frac{-\pi D^2 W_\text{v}\alpha_M p_\text{v}}{R_\text{p}T}\left(\frac{R_\text{m}T}{2W_\text{v}}\right)^{0.5}\,, \tag{5}$$

where α_M is the mass accommodation coefficient, p_v is the partial pressure of sublimed carbon clusters, and R_p and R_m are the universal gas constant expressed in different units. Values of p_v, W_v, ΔH_v, and α_M are given in Table 3.

2.1.4 Conduction. In the Melton model [16] the conductive-cooling rate is calculated for a transition regime according to the approach of McCoy and Cha [45], i.e.

$$\dot{Q}_{\text{Conduction}} = \frac{2\kappa_\text{a}\pi D^2}{D+GL}(T-T_0)\,, \tag{6}$$

where κ_a is the thermal conductivity of the surrounding gases, L is the mean free path, and T_0 is the temperature of the ambient gases. The heat-transfer factor G is given by

$$G = \frac{8f}{\alpha_\text{T}(\gamma+1)}\,, \tag{7}$$

where α_T is the thermal accommodation coefficient (Table 4), γ is the heat-capacity ratio C_p/C_v (Table 4), C_p is the heat capacity of air at constant pressure, and C_v is the heat capacity of air at constant volume. The symbol f represents the Eucken correction to the thermal conductivity given by

$$f = \frac{9\gamma-5}{4}\,. \tag{8}$$

2.1.5 Radiation. The original Melton model [16] also accounts for radiative cooling, but the contribution to the particle temperature from this term is negligible at an ambient pressure of 1 bar and is neglected in the fully constrained model calculations prepared for this comparison. This term is, however, included in the independent model calculations described below.

2.1.6 Solution. The temperature and diameter of the particle as a function of time are derived by solving the differential equations for temperature

$$\frac{\text{d}T}{\text{d}t} = \frac{6}{\pi D^3 \varrho_\text{s} c_\text{s}}\left[\dot{Q}_{\text{Absorption}} - \dot{Q}_{\text{Sublimation}} - \dot{Q}_{\text{Conduction}}\right] \tag{9}$$

and mass using (5). Mass is converted to diameter via

$$D = \left[\frac{6M}{\pi\varrho_\text{s}}\right]^{\frac{1}{3}}\,. \tag{10}$$

The differential equations are solved numerically.

2.1.7 Signal. The signal is calculated according to the Planck function integrated over all solid angles, i.e.

$$S = \varepsilon_{\lambda_\text{s}}\frac{2\pi^2 D^2 hc^2}{\lambda_\text{s}^5\left[\exp\left(\frac{hc}{\lambda_\text{s}k_\text{B}T}\right)-1\right]}\,, \tag{11}$$

where h is the Planck constant, c is the speed of light, k_B is the Boltzmann constant, and λ_s is the emission wavelength. The emissivity is assumed to be

Model	p_v (atm)	W_v (g/mol)	ΔH_v (J/mol)	α_M
Melton [16] (original)	Clausius–Clapeyron eqn[c,d]	36	7.78×10^5	1
Melton (workshop)	Clausius–Clapeyron eqn[c,e]	36, 12 for W_s	7.78×10^5	1
Semi-constrained				1
Bladh	T-dependent[a]	T-dependent[h]	T-dependent[i]	0.8 [35]
Boiarciuc	T-dependent[a]	T-dependent[h]	T-dependent[i]	0.8 [35]
Charwath	Antoine equation[b]	36	7.125×10^5	0.9 [26]
Dreier	Clausius–Clapeyron eqn[c,f]	36	7.9078×10^5 [51]	1
Hadef	Clausius–Clapeyron eqn[c,e]	T-dependent[h]	T-dependent[i]	0.5 [27]
Hofmann	T-dependent[a]	T-dependent[h]	T-dependent[i]	1
Kock	Clausius–Clapeyron eqn[c,f]	36.033	7.9078×10^5 [51]	1
Liu	T-dependent[a]	T-dependent[h]	T-dependent[i]	0.77 [62]
Michelsen	Clausius–Clapeyron eqn[c,g] for each cluster species C_i	$W_i = 12.011i$ for each cluster C_i	Calculated for each cluster C_i^j	C, C_2: 0.5, C_3: 0.1, C_4,C_5: 1×10^{-4} [63]
Will	T-dependent[a]	T-dependent[h]	T-dependent[i]	1

[a] $p_v = \exp(-122.96 + 9.0558 \times 10^{-2} T - 2.7637 \times 10^{-5} T^2 + 4.1754 \times 10^{-9} T^3 - 2.4875 \times 10^{-13} T^4)$ from fits to data by Leider et al. [51]
[b] $p_v = p_{ref} \exp\left(-\frac{37\,500\ \mathrm{K}}{T} + 9.579\right)$ where $p_{ref} = 1$ atm [64]
[c] $p_v = p_{ref} \exp\left[-\frac{\Delta H_v}{R}\left(\frac{1}{T} - \frac{1}{T_{ref}}\right)\right]$
[d] $p_{ref} = 1$ atm; $T_{ref} = 3915$ K from fits to data by Leider et al. [51]
[e] $p_{ref} = 1$ bar; $T_{ref} = 3915$ K
[f] $p_{ref} = 61.50$ Pa; $T_{ref} = 3000$ K from fits to data by Leider et al. [51]
[g] $p_{ref} = 1$ atm; $T_{ref} = 4603.48$ K for C, 4456.59 K for C_2, 4136.78 K for C_3, 4949.74 K for C_4, 4772.87 K for C_5 from fits to data from NIST-JANAF [46]
[h] $W_v = 17.179 + 6.8654 \times 10^{-4} T + 2.9962 \times 10^{-6} T^2 - 8.5954 \times 10^{-10} T^3 + 1.0486 \times 10^{-13} T^4$ from fits to data by Leider et al. [51]
[i] $\Delta H_v = 2.05398 \times 10^5 + 7.3660 \times 10^2 T - 0.40713 T^2 + 1.1992 \times 10^{-4} T^3 - 1.7946 \times 10^{-8} T^4 + 1.0717 \times 10^{-12} T^5$ from fits to data by Leider et al. [51]
[j] $\Delta H_1 = 7.266 \times 10^5 - 5.111T$; $\Delta H_2 = 8.545 \times 10^5 - 12.326T$; $\Delta H_3 = 8.443 \times 10^5 - 26.921T$; $\Delta H_4 = 9.811 \times 10^5 - 7.787T - 2.114 \times 10^{-3} T^2$; $\Delta H_5 = 9.898 \times 10^5 - 7.069T - 2.598 \times 10^{-3} T^2$ from fits to data from NIST-JANAF [46]

TABLE 3 Parameters for $\dot{Q}_{Sublimation}$

Model	α_T	γ (1800 K)
Melton [16] (original)	0.9	1.4
Melton (workshop)	0.3	1.3
Semi-constrained	0.3	
Bladh	0.3 [36, 65–67]	1.3042[a] [36]
Boiarciuc	0.37 [38]	1.3
Charwath	0.28 [26]	1.3
Dreier	0.23	1.3075[b] [30]
Hadef	0.3 [36, 65–67]	1.3042[a] [36]
Hofmann	0.3	1.3075[b] [30]
Kock	0.23	1.3075[b] [30]
Liu	0.37 [38]	1.2660[c] [39]
Michelsen	0.3 [36, 65–67]	1.3042[a] [36]
Will	0.275 [68]	1.3009 [46]

TABLE 4 Parameters for $\dot{Q}_{Conduction}$

[a] $C_p = R\left\{3.498\left(\frac{1\ \mathrm{K}}{T}\right)^2 \exp\left(\frac{1\ \mathrm{K}}{T}\right)\left[\exp\left(\frac{1\ \mathrm{K}}{T}\right) - 1\right]^{-2} + 0.98378\left(\frac{3353.5\ \mathrm{K}}{T}\right)^2 \exp\left(\frac{3353.5\ \mathrm{K}}{T}\right)\left[\exp\left(\frac{3353.5\ \mathrm{K}}{T}\right) - 1\right]^{-2} + \frac{T}{38\,811\ \mathrm{K}}\right\}$ from a fit to data from NIST-JANAF [46], and $\gamma = \frac{C_p}{C_p - R}$
[b] $C_p = 28.58\ \mathrm{J/mol\,K} + 3.77 \times 10^{-3}\ \mathrm{J/mol\,K^2}\,T - \frac{5 \times 10^4\ \mathrm{J\,K/mol}}{T^2}$ [30], and $\gamma = \frac{C_p}{C_p - R}$
[c] $\gamma = 1.4221 - 1.8636 \times 10^{-4} T + 8.0784 \times 10^{-8} T^2 - 1.6425 \times 10^{-11} T^3 + 1.2750 \times 10^{-15} T^4$ [39]

$$\varepsilon_{\lambda_s} = \frac{4\pi D E(m)}{\lambda_s}, \tag{12}$$

which yields

$$S = \frac{8\pi^3 D^3 h c^2 E(m)}{\lambda_s^6 \left[\exp\left(\frac{hc}{\lambda_s k_B T}\right) - 1\right]}, \tag{13}$$

when substituted into (11). For this comparison the signal is calculated at a single emission wavelength of 500 nm.

2.2 *Description of the independent models*

As in the Melton model, in all of the independent models the laser-induced incandescence signal is calculated by solving the energy- and mass-balance equations for particle temperature and size. The energy-balance equation is similarly expressed as a rate equation for energy loss and gain, i.e.

$$\frac{dU_{Internal}}{dt} = \dot{Q}_{Absorption} - \dot{Q}_{Radiation} - \dot{Q}_{Sublimation} - \dot{Q}_{Conduction} + \dot{Q}_{Oxidation} - \dot{Q}_{Thermionic}, \tag{14}$$

as a function of time, temperature, mass, and primary particle diameter.

2.2.1 Internal energy. All of the models except for those of Hofmann and Kock use (2) to express the rate of change of the particle internal energy. In the models of Hofmann and Kock, it is implicitly assumed that $U_{\text{Internal}} = \varrho_{\text{s}} c_{\text{s}} \pi D^3 T/6$, such that the time variation of the particle internal energy can be written as

$$\frac{\mathrm{d}U_{\text{Internal}}}{\mathrm{d}t} = \frac{\mathrm{d}\left(\varrho_{\text{s}} c_{\text{s}} \frac{\pi}{6} D^3 T\right)}{\mathrm{d}t} = \frac{\pi D^3 \varrho_{\text{s}}}{6}\left(c_{\text{s}} + T\frac{\mathrm{d}c_{\text{s}}}{\mathrm{d}T} + \frac{c_{\text{s}}}{\varrho_{\text{s}}} T \frac{\mathrm{d}\varrho_{\text{s}}}{\mathrm{d}T}\right)\frac{\mathrm{d}T}{\mathrm{d}t} + c_{\text{s}} T \frac{\mathrm{d}M}{\mathrm{d}t}\,. \tag{15}$$

The first term of (15) is equivalent to (2). The models of Hofmann and Kock include the first, second, and last terms in this expression but assume that ϱ_{s} does not vary with temperature and thus exclude the third term in (15). There is currently some debate in the community about whether (2) or (15) is the correct expression to use. Values of ϱ_{s} and c_{s} used in the models are shown in Fig. 3 and given in Table 1. Several models (Dreier, Hofmann, Kock, Will) use temperature-dependent fits to tabulated values of c_{s} taken from the NIST-JANAF compendium of reference data [30, 46]. Other models (Bladh, Hadef, Michelsen) use a temperature-dependent parameterization from Fried and Howard [36, 47], which is indistinguishable from the NIST-JANAF tabulations. The Liu model uses an alternative temperature-dependent formulation. The Bladh, Hadef, and Michelsen models also use temperature-dependent values of ϱ_{s} from fits to values given by Fried and Howard [36, 47].

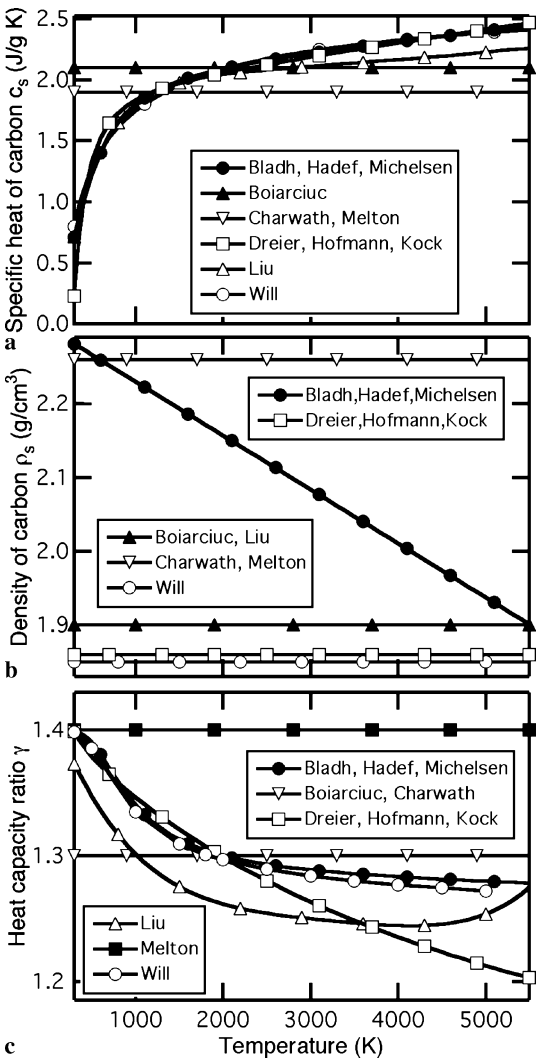

FIGURE 3 Temperature dependence of selected parameters. The (**a**) specific heat (Table 1) and (**b**) density (Table 1) of the particle and (**c**) heat-capacity ratio of the surrounding gases (Table 4) are shown as a function of temperature. Values used in the different models are indicated in the legend in each panel

2.2.2 Absorption. Eight of the ten models in the comparison use the Rayleigh approximation given in (3) to calculate the absorptive-heating rate. The absorption rate in the Will model is calculated using full Mie theory without a Rayleigh approximation [48]. Values of $E(m)$ used in the models are given in Table 2. The Michelsen model uses an alternative expression, which accounts for saturation of the linear, single-photon absorption, and multiphoton absorption leading to C_2 photodesorption at high fluence. This expression is written as

$$\dot{Q}_{\text{Absorption}} = \frac{\pi D^2 \varepsilon_\lambda}{4}\frac{B_{\lambda 1} f_1}{q_1}\left\{1 - \exp\left[-\frac{q\,(t)\,F}{B_{\lambda 1}}\right]\right\} + \frac{\sigma_{\lambda n}\pi D^3 N_{\text{ss}}}{6}\frac{B_{\lambda n}^n}{q_n}\left\{1 - \exp\left[-\left(\frac{q(t)F}{B_{\lambda n}}\right)^n\right]\right\}\,, \tag{16}$$

where q_n normalizes the integrated nth power of the laser temporal profile to unity, $\sigma_{\lambda n}$ is a multiphoton absorption cross section, n is the number of photons absorbed, $B_{\lambda 1}$ and $B_{\lambda n}$ are saturation coefficients for linear and multiphoton absorption, f_1 is an empirical scaling factor for linear absorption, and N_{ss} is the density of carbon atoms on the surface of the particle.

2.2.3 Radiation. All of the models integrate the Planck function over all wavelengths to calculate the rate of radiative emission from the particle, i.e.

$$\dot{Q}_{\text{Radiation}} = \pi D^2 \int_0^\infty \varepsilon_\lambda \frac{2\pi h c^2}{\lambda'^5\left[\exp\left(\frac{hc}{\lambda' k_{\text{B}} T}\right) - 1\right]}\,\mathrm{d}\lambda'\,. \tag{17}$$

Five of the ten models in the comparison (Bladh, Charwath, Liu, Michelsen, Will) use the Rayleigh approximation for the emissivity, as given by (12). Performing the integration in (17) thus yields

$$\dot{Q}_{\text{Radiation}} = \frac{199\pi^3 D^3 (k_{\text{B}} T)^5 E(m)}{h(hc)^3}\,, \tag{18}$$

if $E(m)$ is wavelength independent. Several of the models (Charwath, Michelsen, Will) account for re-absorption of background emission by subtracting $\dot{Q}_{\text{Radiation}}(T_0)$ from (18). Two of the models (Hofmann, Kock) use the approximation of

a perfect black body in which (17) is solved with an emissivity of 1, yielding

$$\dot{Q}_{\text{Radiation}} = \pi D^2 \sigma_{\text{SB}} \left(T^4 - T_0^4\right) , \tag{19}$$

where σ_{SB} is the Stefan–Boltzmann constant and T_0 is the ambient temperature, which accounts for absorption of radiative emission from the surrounding gases. Two of the models (Boiarciuc, Dreier) attempt to account for the wavelength dependence of the emissivity by multiplying (19) by the emissivity given in (12) and performing a second integration over wavelength. One of the models (Hadef) uses an expression for radiative cooling in which the emissivity at a wavelength λ is given by [49, 50]

$$\varepsilon_\lambda = \frac{2\beta D}{3\lambda^\xi} . \tag{20}$$

Here the exponent ξ is used to account for deviations from a $1/\lambda$ dependence observed in the visible and near-infrared regions, and β is a scaling factor. Substituting this emissivity into (17) and performing the integration yields [36]

$$\dot{Q}_{\text{Radiation}} = \frac{25.90\beta\pi^2 D^3 (k_{\text{B}}T)^{4+\xi}}{h(hc)^{2+\xi}} . \tag{21}$$

This equation can be rewritten in the format of (18) if $E(m) = \frac{0.13\beta}{\pi}\left(\frac{k_{\text{B}}T}{hc}\right)^{\xi-1}$.

2.2.4 Sublimation. Nine of the ten models in the comparison represent the evaporative-cooling rate as

$$\dot{Q}_{\text{Sublimation}} = -\frac{\Delta H_{\text{v}}}{W_{\text{v}}}\frac{\text{d}M}{\text{d}t} . \tag{22}$$

In eight of these models the mass loss via sublimation is given as

$$\frac{\text{d}M}{\text{d}t} = \frac{-\pi D^2 W_{\text{v}} \alpha_{\text{M}} p_{\text{v}}}{R_{\text{p}} T}\left(\frac{R_{\text{m}}T}{2\pi W_{\text{v}}}\right)^K . \tag{23}$$

For two of these models (Charwath, Hadef) K has the value of 0.4 to account for the non-ideality of the ambient gases and desorbed clusters [26, 27]. The other models use a value of 0.5. Values used for the mass accommodation coefficient α_{M}, average partial pressure p_{v}, average mass W_{v}, and average enthalpy of formation ΔH_{v} of sublimed carbon clusters are given in Table 3. The Hofmann model uses (22) to represent evaporative cooling but accounts for the reduction in carbon cluster flux from the surface under high-pressure conditions by expressing mass loss as [18]

$$\frac{\text{d}M}{\text{d}t} = \frac{-\pi D^2 W_{\text{v}}}{N_{\text{A}}}\left(\frac{1}{N_{\text{FM}}} + \frac{1}{N_{\text{C}}}\right)^{-1} . \tag{24}$$

Here N_{A} is the Avogadro constant. The flux term for the free molecular flow regime is given as

$$N_{\text{FM}} = \frac{\alpha_{\text{M}} p_{\text{v}}}{k_{\text{p}} T}\left(\frac{R_{\text{m}}T}{2\pi W_{\text{v}}}\right)^{0.5} , \tag{25}$$

and the flux term for the continuum regime can be written as

$$N_{\text{C}} = \frac{f k_{\text{p}} T}{\sqrt{2}\bar{\sigma}\, p_0 D}\frac{p_{\text{v}}}{k_{\text{p}}T}\left(\frac{R_{\text{m}}T}{2\pi W_{\text{v}}}\right)^{0.5} = \frac{f k_{\text{p}} T}{\sqrt{2}\bar{\sigma}\, p_0 D\alpha_{\text{M}}} N_{\text{FM}} , \tag{26}$$

where p_0 is the ambient pressure, k_{p} is the Boltzmann constant in effective pressure units, and $\bar{\sigma}$ is an average molecular cross section for subliming species. Equation (24) can be rewritten as

$$\frac{\text{d}M}{\text{d}t} = \frac{-\pi D^2 W_{\text{v}} \alpha_{\text{M}} p_{\text{v}}}{R_{\text{p}} T}\left(\frac{R_{\text{m}}T}{2\pi W_{\text{v}}}\right)^{0.5} \times \left(\frac{f k_{\text{p}} T}{\sqrt{2}\bar{\sigma}\, p_0 D\alpha_{\text{M}} + f k_{\text{p}} T}\right) , \tag{27}$$

which is equivalent to (23) when $\sqrt{2}\bar{\sigma}\, p_0 D\alpha_{\text{M}} \ll f k_{\text{p}} T$.

Six of these models (Bladh, Boiarciuc, Hadef, Hofmann, Liu, Will) use temperature-dependent parameterizations derived from data presented by Leider et al. [51] for the average mass and enthalpy of formation, and five of these models use similarly derived average equilibrium partial pressures [35]. The Charwath model uses the Antoine equation [26, 27], and the other four models (Dreier, Hadef, Kock, Michelsen) use the Clausius–Clapeyron equation [30, 36] to calculate equilibrium partial pressures based on data from Leider et al. [51] (Dreier, Kock) or from the NIST-JANAF tables [46] (Michelsen). Three of the models (Charwath, Dreier, Kock) assume that the only species to sublime is C_3 and use the corresponding molecular weight and enthalpy of formation. These parameterizations are summarized in Table 3. The Michelsen model calculates $\dot{Q}_{\text{Sublimation}}$ independently for each carbon cluster from C_1 to C_5 [36]. In this model the evaporative-cooling term includes a contribution from photodesorption of C_2 and is expressed as

$$\dot{Q}_{\text{Sublimation}} = -\sum_{j=1}^{5}\frac{1}{W_j}\left(\frac{\text{d}M}{\text{d}t}\right)_j \times \left[\frac{\Delta H_j\left(p_{\text{sat}}^{C_j} - p_{\lambda n}\right) + \Delta H_{\lambda n} p_{\lambda n}}{p_{\text{sat}}^{C_j}}\right] , \tag{28}$$

where the summation is over contributions to $\dot{Q}_{\text{Sublimation}}$ from each desorbed carbon cluster species C_j with molecular weight W_j and heat of formation ΔH_j. The saturation partial pressure of C_j $\left(p_{\text{sat}}^{C_j}\right)$ depends on thermal (sublimation) and non-thermal (photodesorption) vaporization rates. Assuming that only C_2 is produced by photolysis, any non-thermal photodesorption of C_2 will contribute to its instantaneous surface pressure. If the effective pressure from this non-thermal mechanism exceeds the thermal equilibrium partial pressure $p_{\text{v}}^{C_j}$, thermal desorption of clusters will cease. The effective instantaneous pressure will then be equal to $p_{\lambda n}$, the partial pressure of C_2 produced by direct photolytic production. If $p_{\lambda n}$ is small compared to $p_{\text{v}}^{C_j}$ (e.g. after the laser pulse if the particle temperature is still high), the instantaneous partial pressure of C_2 at the surface of the particle will be determined

by $p_{\mathrm{v}}^{C_j}$. When $j = 2$, the photolytic contribution to the partial pressure is given by

$$p_{\lambda n} = \frac{k_{\mathrm{p}} T k_{\lambda n}}{\pi D^2 \alpha_j U_j}\,, \tag{29}$$

where α_j is the mass accommodation coefficient. For cluster species other than C_2, $p_{\lambda n}$ is zero. The rate constant is expressed as

$$k_{\lambda n} = \frac{\lambda}{nhc}\frac{\sigma_{\lambda n}\pi D^3 N_{\mathrm{ss}}}{6}\frac{B_{\lambda n}^n}{q_n}\left\{1-\exp\left[-\left(\frac{q(t)F}{B_{\lambda n}}\right)^n\right]\right\}\,, \tag{30}$$

and the average thermal velocity of the carbon cluster species (C_2 in this case) diffusing away from the surface is given as

$$U_j = \sqrt{\frac{R_{\mathrm{m}}T}{2\pi W_j}}\,. \tag{31}$$

For each carbon cluster species the rate of mass loss during sublimation is given by

$$\left(\frac{\mathrm{d}M}{\mathrm{d}t}\right)_j = \frac{-\pi D^2 W_j U_j \alpha_j B_j}{R_{\mathrm{p}}T}\,, \tag{32}$$

where the convective contributions to the heat and mass transfer from the particle to the surrounding atmosphere (Stefan flow) are contained in the factor B_j. Further details about B_j are given elsewhere [36].

2.2.5 Conduction. At an ambient pressure of 1 bar and a temperature of 1800 K the mean free path greatly exceeds the particle size, and the conductive-cooling rate is calculated in seven of the models (Charwath, Dreier, Hadef, Hofmann, Kock, Liu, Michelsen) assuming a free molecular flow regime, i.e.

$$\dot{Q}_{\mathrm{Conduction}} = \frac{\pi D^2 \alpha_{\mathrm{T}} p_0}{2T_0}\sqrt{\frac{R_{\mathrm{m}}T_0}{2\pi W_{\mathrm{a}}}}\left(\frac{\gamma+1}{\gamma-1}\right)(T-T_0)\,, \tag{33}$$

which is equivalent to

$$\dot{Q}_{\mathrm{Conduction}} = \frac{\pi D^2 \alpha_{\mathrm{T}} p_0}{R_{\mathrm{p}}T_0}\sqrt{\frac{R_{\mathrm{m}}T_0}{2\pi W_{\mathrm{a}}}}\left(C_{\mathrm{p}}-\frac{R}{2}\right)(T-T_0)\,, \tag{34}$$

if γ is evaluated at the gas temperature. In the above equations W_{a} is the molecular weight of air. Three models implement a transition-regime approximation based on the Fuchs method [39, 54] (Bladh) or the McCoy and Cha [45] approach (Boiarciuc, Will) outlined in (6)–(8). Several of the models (Dreier, Hadef, Hofmann, Kock, Liu, Michelsen) assume free molecular flow at low pressure and switch to a transition or continuum regime at higher pressure. Free molecular flow is assumed for $L >\sim 5D\sqrt{\frac{\gamma\pi}{2}}$ [52, 53] (i.e. $p_0 <\sim 3$ bar at 1800 K for a 30-nm-diameter particle) in the Hadef and Michelsen models. The switch occurs at higher pressures ($\sim$ 15 bar at 1800 K for a 30-nm particle) in the Liu model [39]. Equation (6) can be shown to be equivalent to (33) or (34) when $GL \gg D$ (i.e. free molecular flow conditions) using a mean free path of

$$L = \frac{\kappa_{\mathrm{a}}T_0}{2fp_0}(\gamma-1)\sqrt{\frac{2\pi W_{\mathrm{a}}}{R_{\mathrm{m}}T_0}} \tag{35}$$

or

$$L = \frac{k_{\mathrm{P}}T_0}{\sqrt{2}\sigma P_0} \tag{36}$$

and a thermal conductivity of

$$\kappa_{\mathrm{a}} = \frac{4C_{\mathrm{p}}+5R}{4\sigma N_{\mathrm{A}}}\sqrt{\frac{R_{\mathrm{m}}T_0}{\pi W_{\mathrm{a}}}} = \frac{fR}{(\gamma-1)\,\sigma N_{\mathrm{A}}}\sqrt{\frac{R_{\mathrm{m}}T_0}{\pi W_{\mathrm{a}}}}\,, \tag{37}$$

where σ is the average molecular cross section of air.

Values of α_{T} and γ are given in Table 4, and γ is shown as a function of temperature in Fig. 3c. For this comparison the temperature dependence of γ is not generally relevant because calculations were performed at a constant ambient temperature of 1800 K for which values of γ are given in Table 4. The Hofmann and Liu models, however, use (33) with values for γ that rely on particle temperature. In these models γ is replaced by γ^*, where [39, 54]

$$\frac{1}{\gamma^*-1} = \frac{1}{T-T_0}\int_{T_0}^{T}\frac{\mathrm{d}T'}{\gamma-1}\,. \tag{38}$$

The Bladh model uses a similar expression with T_0 replaced by T_δ, where T_δ is the temperature in the boundary layer of the particle. Further details are given elsewhere [40].

2.2.6 Oxidation. The Michelsen model also includes heating and mass loss attributable to oxidation. The enhancement in the particle energy by oxidation can be estimated by [36]

$$\dot{Q}_{\mathrm{Oxidation}} = \left(-\Delta H_{\mathrm{ox}} - 2\alpha_{\mathrm{T}}C_{\mathrm{P}}^{\mathrm{CO}}T\right)\frac{\pi D^2 k_{\mathrm{ox}}}{N_{\mathrm{A}}}\,, \tag{39}$$

assuming production of CO from the surface reaction of C + O_2 and partial accommodation of CO with the surface prior to desorption. For this calculation k_{ox} is the reaction rate of molecular oxygen with the surface, ΔH_{ox} is the enthalpy of reaction, and $C_{\mathrm{P}}^{\mathrm{CO}}$ is the molar heat capacity of CO at the surface temperature. This term is zero for the other models. The rate of mass loss caused by oxidation is estimated as

$$\left(\frac{\mathrm{d}M}{\mathrm{d}t}\right)_{\mathrm{ox}} = -\frac{2\pi D^2 W_1 k_{\mathrm{ox}}}{N_{\mathrm{A}}}\,. \tag{40}$$

The model incorporates a parameterization for k_{ox} (described in more detail elsewhere [36]) assuming a partial pressure for O_2 of $0.21P_0$.

2.2.7 Thermionic emission. The Michelsen model includes cooling by thermionic emission in which electrons are thermally ejected from the particle. This term is expressed

based on a Richardson–Dushman approximation according to [33, 55]

$$\dot{Q}_{\text{Thermionic}} = \frac{4\phi m_{\text{e}}\,(\pi D k_{\text{B}} T)^2}{h^3} \exp\left(\frac{-\phi}{k_{\text{B}} T}\right), \tag{41}$$

where ϕ is the work function and m_{e} is the electron mass.

2.2.8 Solution. The time dependence of the temperature and diameter of the particle are calculated by solving the coupled differential equations for temperature and mass using

$$\frac{\mathrm{d}U_{\text{Internal}}}{\mathrm{d}t} = \left(\dot{Q}_{\text{Absorption}} - \dot{Q}_{\text{Radiation}} - \dot{Q}_{\text{Sublimation}} - \dot{Q}_{\text{Conduction}} + \dot{Q}_{\text{Oxidation}} - \dot{Q}_{\text{Thermionic}}\right) \tag{42}$$

and (23) (Bladh, Boiarciuc, Charwath, Dreier, Hadef, Kock, Liu, Will), (27) (Hofmann), or

$$\frac{\mathrm{d}M}{\mathrm{d}t} = \sum_{j=1}^{5} \left(\frac{\partial M}{\partial t}\right)_j + \left(\frac{\partial M}{\partial t}\right)_{\text{ox}} \tag{43}$$

(Michelsen).

The differential equations are solved numerically in most of the models using a first-order Euler method (Liu, Will) or fourth-order (Bladh, Boiarciuc, Charwath, Dreier, Hadef, Hofmann, Michelsen) or second-order (Kock) Runge–Kutta methods. The models use time steps of 1 ps (Will), 5 ps (Hadef), 20 ps (Charwath), 50 ps (Michelsen), 100 ps (Dreier, Kock, Liu), 200 ps (Hofmann), or variable up to 400–600 ps (Bladh, Boiarciuc).

2.2.9 Signal. For this comparison the signal is calculated according to (13) at a wavelength of 500 nm with values of $E(m)$ given in Table 3.

3 Results and discussion

3.1 *Calculations using the fully constrained model*

As expected, excellent agreement was achieved among the results from the fully constrained model. Figure 4 shows ten sets of calculated temperatures and LII signals for a fluence of 0.05 J/cm^2. The results overlap, making them indistinguishable. At low fluence in this model, temperatures are not high enough to lead to sublimation, and the predicted particle size is a constant value of 30 nm. Conductive cooling is responsible for the signal decay. Figure 5 shows calculated temperatures, diameters, and signals for a fluence of 0.70 J/cm^2. Again the results are indistinguishable from one another and appear as a single line. At this fluence sublimation leads to mass loss and contributes to the signal decay rate via particle-size reduction and evaporative cooling. The results for each fluence from nine of the ten sets of calculations agree to within 1% of the mean over most of the temporal profile. Larger percent deviations occur prior to the appearance of the LII signal at very low signal levels and depend on how the initial luminosity from the 1800-K particle is treated. The Boiarciuc signal calculations diverge slowly from the others with time and are $\sim 3.5\%$ lower than the mean at 500 ns. This level of agreement among the model runs verifies that the calculations from the different groups are being performed consistently.

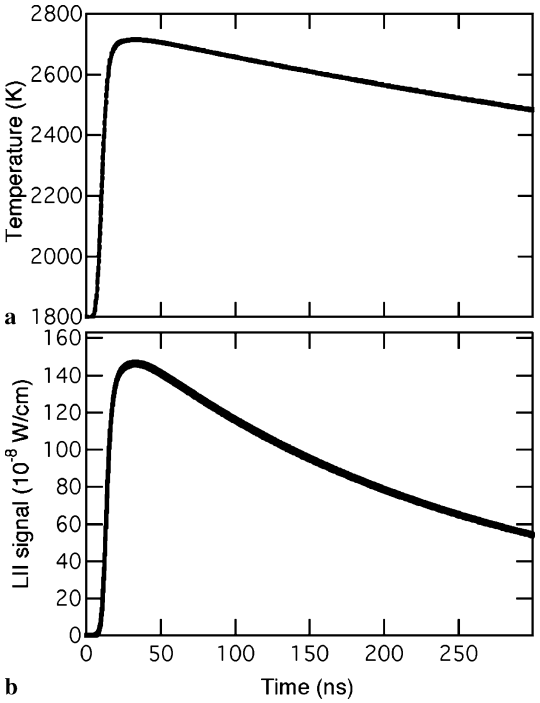

FIGURE 4 Comparison of modeled temperature and LII signal from the fully constrained model. Results of ten sets of calculated (**a**) temperatures and (**b**) LII signals are shown as a function of time. Calculations were performed for a fluence of 0.05 J/cm^2

3.2 *Calculations using independent, unconstrained models for low fluence*

Figure 6 shows temperatures, diameters, and LII signals produced by the independent models with unconstrained parameters for a fluence of 0.05 J/cm^2. Peak temperatures are largely determined by the absorptive-heating rate $\dot{Q}_{\text{Absorption}}$ shown in Fig. 7a. According to (3), $\dot{Q}_{\text{Absorption}}$ should be linearly dependent on $E(m)$. Nine of the models use this expression for $\dot{Q}_{\text{Absorption}}$. Figure 8a shows peak values of $\dot{Q}_{\text{Absorption}}$ as a function of $E(m)$, demonstrating a linear dependence for these nine models. In the Michelsen model the value of $\dot{Q}_{\text{Absorption}}$ is much larger than in the other models because it includes a nonlinear absorption term for multiphoton photodesorption.

Because peak temperatures are predominantly determined by $\dot{Q}_{\text{Absorption}}$, they should also be correlated with $E(m)$, as shown in Fig. 8b. This correlation suggests that much of the spread in temperatures shown in Fig. 6a is attributable to the range of values used for $E(m)$. Despite the large positive deviation from the correlation between the peak $\dot{Q}_{\text{Absorption}}$ and $E(m)$ demonstrated by the Michelsen model in Fig. 8a, the peak temperature demonstrates a negative deviation from the correlation with $E(m)$ in Fig. 8b. This difference has two causes. First, the nonlinear absorption term that enhances $\dot{Q}_{\text{Absorption}}$ (Fig. 8a) does not contribute significantly to particle heating. Most of the energy from the additional photons absorbed leads directly to photodesorption of C_2 prior to thermalization with the particle. Second, the Michelsen model

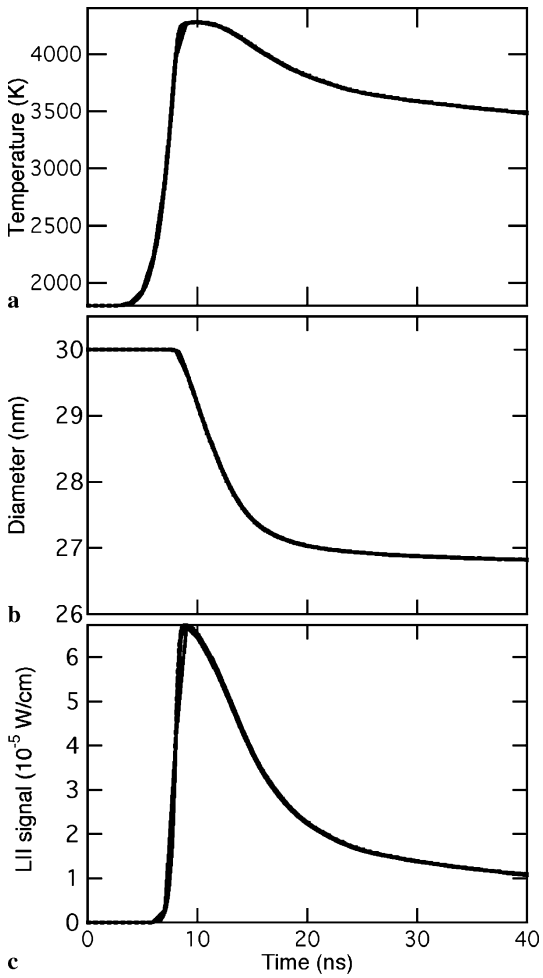

FIGURE 5 Comparison of modeled temperature, diameter, and LII signal from the fully constrained model. Results of ten sets of calculated (**a**) temperatures, (**b**) diameters, and (**c**) LII signals are shown as a function of time. Calculations were performed for a fluence of 0.70 J/cm^2

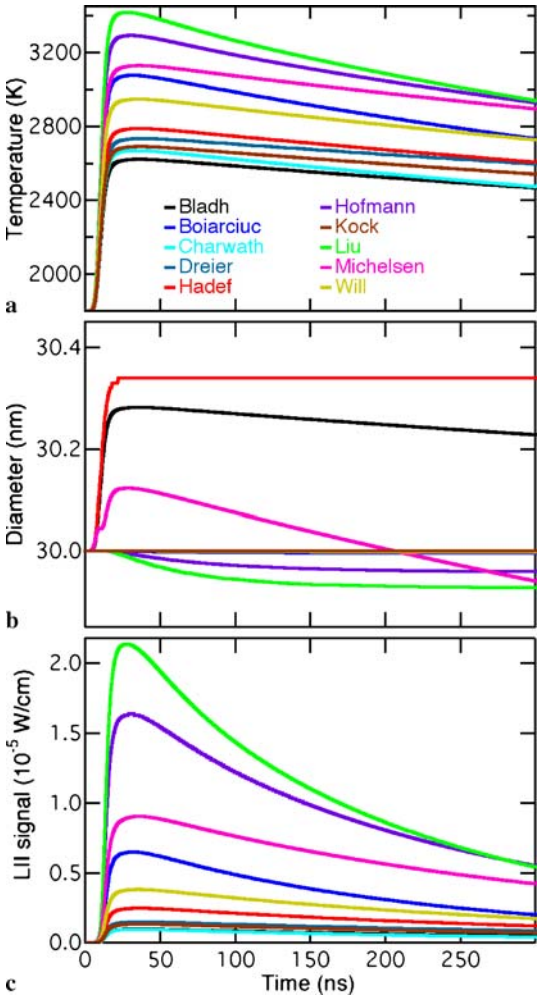

FIGURE 6 Comparison of modeled temperature, diameter, and LII signal from the unconstrained, independent models. Calculated (**a**) temperatures, (**b**) diameters, and (**c**) LII signals are shown as a function of time for ten models identified in the legend. Calculations were performed for a fluence of 0.05 J/cm^2

includes saturation of the linear absorption; at the peak of the laser profile $E(m)$ is effectively $\sim 4\%$ smaller than the nominal value. Accounting for this saturation effect brings the Michelsen model into better agreement with the other models. The Hofmann model also appears to deviate from the correlation in Fig. 8b. This behavior is represented by a reverse order of Hofmann and Liu model results in Figs. 6a and 7a, i.e. the Hofmann model predicts lower temperatures than the Liu model even though the Hofmann values for $\dot{Q}_{\text{Absorption}}$ are higher. These deviations can be explained by differences in the way $\mathrm{d}U_{\text{Internal}}/\mathrm{d}t$ is expressed in the Hofmann model (Sect. 2.2.1). Other deviations from the correlation between peak temperature and $\dot{Q}_{\text{Absorption}}$ and $E(m)$ may similarly be explained by differences in values of soot density used.

At the lower fluence sublimation rates are very low (Fig. 7b), and the particle diameter does not change significantly with time, as shown in Fig. 6b. For the Bladh, Hadef, and Michelsen models the initial increase in the diameter of the particle is attributable to the change in density with temperature. In the Michelsen model the decrease in diameter after 30 ns is caused by oxidation, whereas the decrease in the Bladh model is caused by the decrease in particle temperature and increase in density. The decrease in diameter in the Liu and Hofmann models is caused by sublimation. Photodesorption of C_2 is responsible for the initial higher sublimation rates in the Michelsen model (Fig. 7b), which leads to a small notch during the laser pulse in the diameter evolution in Fig. 6b and a smaller peak diameter than would be anticipated solely from the decrease in density with temperature.

Because particle diameters do not change significantly at low fluence, LII signals are controlled by particle temperatures according to (13). Figure 9 shows the nonlinear but tight correlation between predicted peak LII signal and peak temperature. The line is meant to guide the eye.

Figure 10a demonstrates the wide range of values of $\dot{Q}_{\text{Conduction}}$ calculated for the low-fluence case (from 74% above the mean to 43% below the mean). Under the ambient conditions studied here, the system can be assumed to be in a free molecular flow regime when the sublimation rate is low. Most of the models use a free molecular flow description to calculate the conductive-cooling rate for these conditions. Several of the models (Bladh, Boiarciuc, Will) use a transition-regime expression to calculate the conductive-cooling term. As noted above, however, these transition-

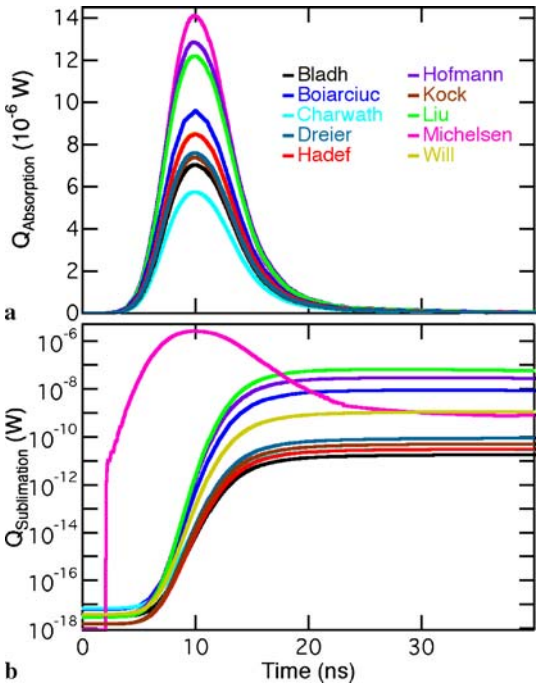

FIGURE 7 Comparison of absorptive-heating and evaporative-cooling rates from the unconstrained, independent models. Calculated values of (**a**) the absorptive-heating rate and (**b**) the evaporative-cooling rate are shown as a function of time for ten models identified in the legend. Calculations were performed for a fluence of 0.05 J/cm^2

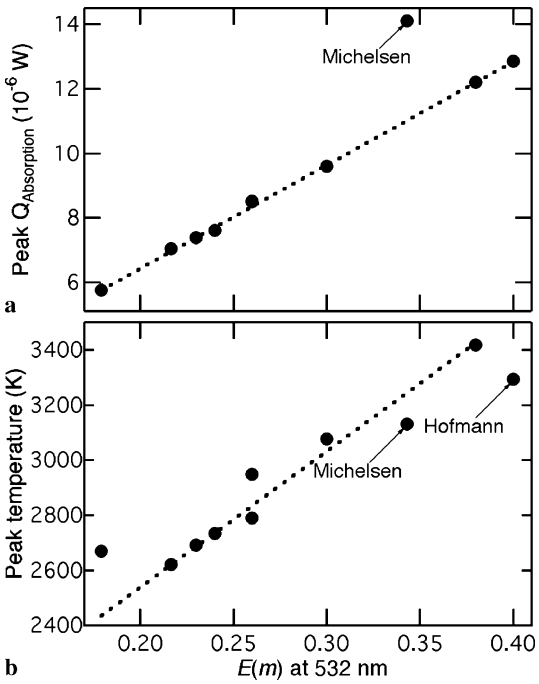

FIGURE 8 Dependence of the absorptive-heating rate and temperature on $E(m)$. The maxima of the (**a**) absorptive-heating rate curves (Fig. 7a) and (**b**) calculated temperature curves (Fig. 6a) are shown as a function of the value of $E(m)$ used in the unconstrained, independent models. Values that deviate from the linear correlations represented by the *dotted lines* are identified by model. Calculations were performed for a fluence of 0.05 J/cm^2

regime expressions can be reduced to the expression used to represent free molecular flow for a 30-nm particle at 1 bar and 1800 K. The main differences between the models are in the choice of the accommodation coefficient and the temperature dependence of the heat capacities or heat-capacity ratio.

In order to isolate the temperature-dependent portion of this expression, we have divided the left-hand side of (33) by the right-hand side of (33) using a constant value of γ ($\gamma_0 = 1.3$) and values of $\dot{Q}_{\text{Conduction}}$ (Fig. 10a), T (Fig. 6a), and D (Fig. 6b) from each model. This parameter manipulation should yield values close to 1, i.e.

$$Q_{\text{Reduced}} = \dot{Q}_{\text{Conduction}} \frac{2T_0}{\pi D^2 \alpha_T p_0} \sqrt{\frac{2\pi W_a}{R_m T_0}} \left(\frac{\gamma_0 - 1}{\gamma_0 + 1}\right) \times \left(\frac{1}{T - T_0}\right) \approx 1\,, \tag{44}$$

and deviations from a constant value of 1 represent the influence of the heat-capacity ratio and the approach used to perform the calculations. The results are shown in Fig. 11 plotted as a function of T. In this analysis most of the models should give a constant value of approximately 1 because they incorporate a value of γ_0 close to 1.3, which was used in (44); most of the models deviate from 1 by $< 2\%$. The Bladh, Hofmann, and Liu models use values of γ that increase with particle temperature (38), which explains the increase in Q_{Reduced} with temperature. Differences between these models may be explained by differences in γ shown in Fig. 3c. The Charwath model also increases with temperature, but the reason is not currently understood.

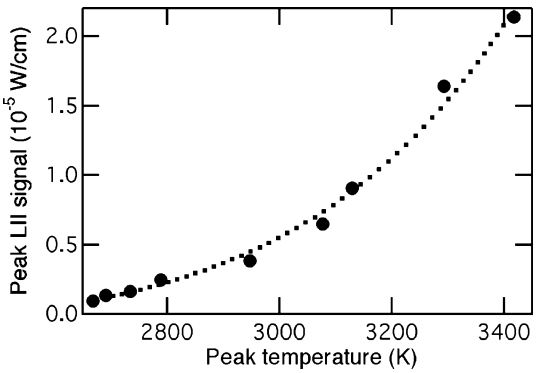

FIGURE 9 Dependence of the LII signal on temperature. The maxima of the calculated signal curves (Fig. 6c) are shown as a function of the maxima of the calculated temperature curves (Fig. 6a) for the unconstrained, independent models. The *dotted line* is meant to guide the eye. Calculations were performed for a fluence of 0.05 J/cm^2

Figure 10b demonstrates a wide range of calculated values for the radiative-cooling rate. These cooling rates are, however, very small compared to those of the other mechanisms and have a negligible effect on the particle temperature. Since the calculations of the broadband radiative emission for the determination of radiative-cooling rates are independent of the single-wavelength calculations used to predict the LII signal in some models, the wide range of values shown in Fig. 10b is not directly reflected in Fig. 6c.

For the conditions studied here, the cooling rate by thermionic emission and the heating rate by oxidation are smaller than the conductive-cooling rate by a factor of ~ 10 in the Michelsen model and have little effect on the calculated signals.

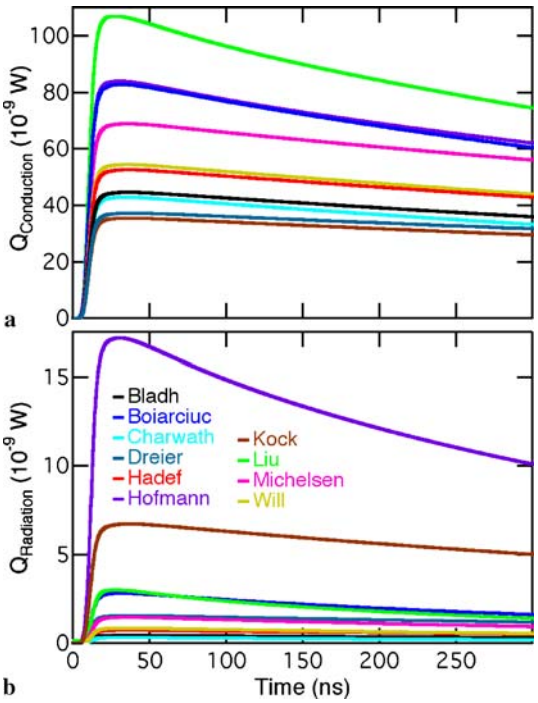

FIGURE 10 Comparison of conductive- and radiative-cooling rates from the unconstrained, independent models. Calculated values of (**a**) the conductive-cooling rate and (**b**) the radiative-cooling rate are shown as a function of time for ten models identified in the legend. Calculations were performed for a fluence of 0.05 J/cm^2

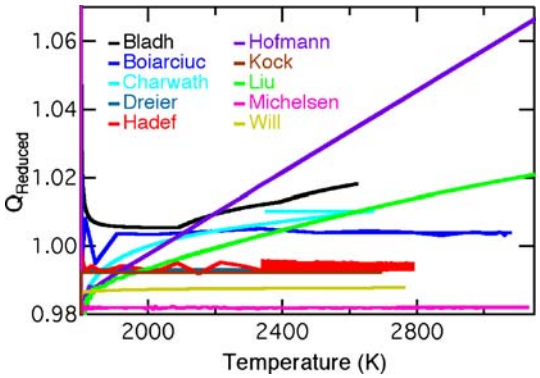

FIGURE 11 Temperature dependence of the conductive-cooling rates in the unconstrained, independent models. In order to isolate the temperature-dependent factors in the calculation of conductive-cooling rates, the results of (44) are shown as a function of temperature for a fluence of 0.05 J/cm^2

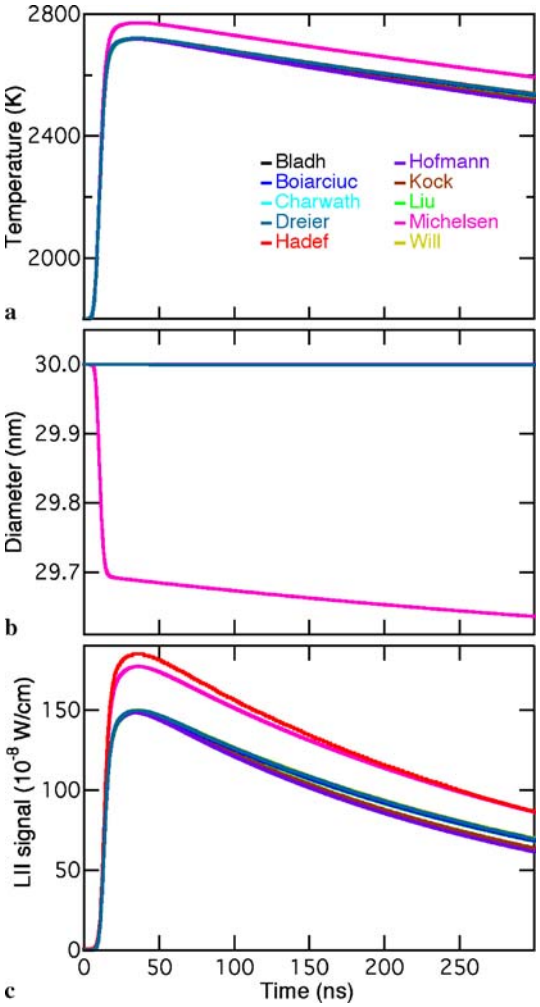

FIGURE 12 Comparison of modeled temperature, diameter, and LII signal from the constrained, independent models. Calculated (**a**) temperatures, (**b**) diameters, and (**c**) LII signals are shown as a function of time for ten models identified in the legend. Calculations were performed for a fluence of 0.05 J/cm^2

3.3 *Calculations using independent, constrained models for low fluence*

The analysis shown in Fig. 11 is one way of isolating the influence of the input parameters (α_T in this case) from that of the modeling approach. Calculations were also performed with constrained input parameters in which all of the models were run with the same values for selected parameters. Figure 12 shows the results of these model runs for a fluence of 0.05 J/cm^2 with constrained values for ϱ_s, c_s, $E(m)$, W_a, α_T, and α_M (see Tables 1–4). This figure corresponds to Fig. 6, which shows the same calculations with unconstrained parameters.

Constraining the parameters reduces the spread in calculated values by a factor of 15 for temperature (from 797 to 52 K at 30 ns) and 60 for LII signal (from 204×10^{-7} to 3.4×10^{-7} W/cm at 30 ns). The decrease in the spread of calculated temperatures can be primarily attributed to constraining $E(m)$, which dramatically reduces the range of values calculated for $\dot{Q}_{Absorption}$ (Fig. 13a compared to Fig. 7a). The strong dependence of peak temperature and $\dot{Q}_{Absorption}$ on $E(m)$ was shown in Fig. 8. The Michelsen model gives higher values for the signal because the calculated temperatures are higher, which in turn can be traced to the additional nonlinear component of the absorption term. The reason for the higher signal from the Hadef model is not clear, however, because temperatures and diameters are the same as those given by most of the other models.

Nine of the ten models yield the same values for $\dot{Q}_{Absorption}$. The Michelsen model produces significantly higher values because of the additional nonlinear absorption leading to photodesorption. The range of values for $\dot{Q}_{Sublimation}$ is also decreased (Fig. 13b compared to Fig. 7b), largely because several of the models (Boiarciuc, Hofmann, Liu, Will) do not predict temperatures as high as they do when unconstrained. As a result these models predict much less change in diam-

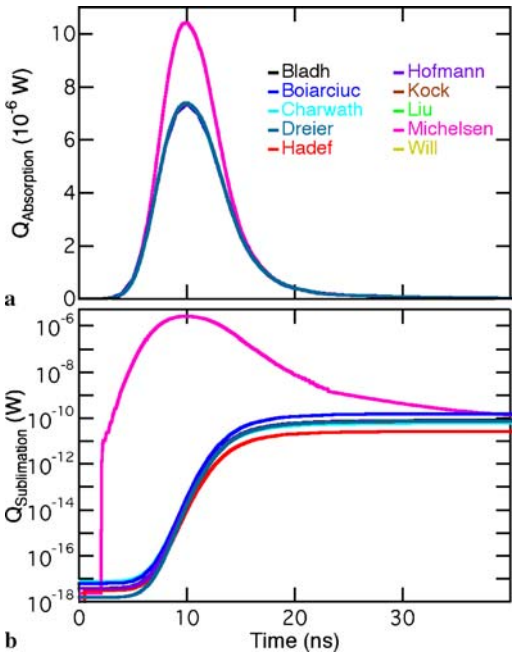

FIGURE 13 Comparison of absorptive-heating and evaporative-cooling rates from the constrained, independent models. Calculated values of (**a**) the absorptive-heating rate and (**b**) the evaporative-cooling rate are shown as a function of time for ten models identified in the legend. Calculations were performed for a fluence of 0.05 J/cm^2

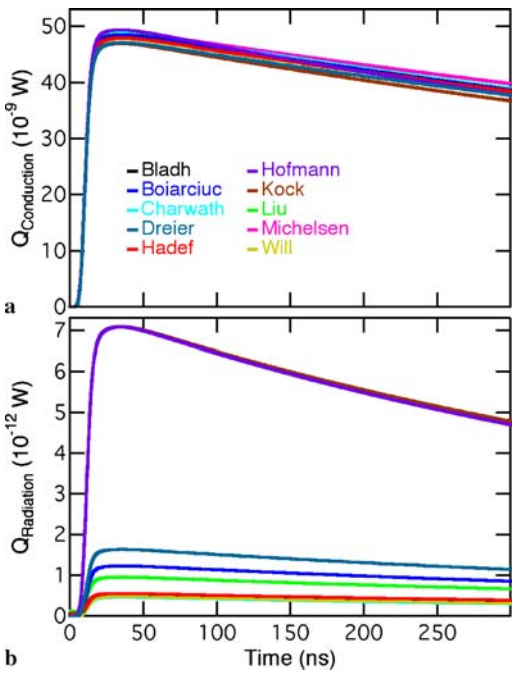

FIGURE 14 Comparison of conductive- and radiative-cooling rates from the constrained, independent models. Calculated values of (**a**) the conductive-cooling rate and (**b**) the radiative-cooling rate are shown as a function of time for ten models identified in the legend. Calculations were performed for a fluence of 0.05 J/cm^2

eter (Fig. 12b) than when unconstrained (Fig. 6b). The initial diameter reduction in the Michelsen model is attributable to photodesorption, and the slower size reduction results from oxidation. The diameter does not increase in this model run because the particle density used in the constrained calculations is independent of temperature.

Constraining parameters also reduces the spread in the conductive-cooling rates (Fig. 14a compared to Fig. 10a). When the same value of α_T is used in all the models, values of $\dot{Q}_{\text{Conduction}}$ range from 2.4% above the mean (Hofmann) to 2.5% below the mean (Kock) near the peak of the profile.

For the radiative-cooling rate (Fig. 14b compared to Fig. 10b) the most significant differences between the models are related to the method used to represent this mechanism. The models that rely on a perfect black-body approximation (Hofmann, Kock) predict a substantially higher radiative-cooling rate than the other models. Models using a modified black-body approximation (Dreier, Boiarciuc) also yield higher values of $\dot{Q}_{\text{Radiation}}$ than the other six models. Five of the models (Bladh, Charwath, Hadef, Michelsen, Will), which use a Rayleigh or modified Rayleigh approximation, are brought into much better agreement (within 8% of the mean) by using the same value of $E(m)$. The Liu model is 71% higher than the average of the other four models because it used a value of 0.4 for $E(m)$ to describe broadband emission, and the other models used a value of 0.23 for the constrained model runs.

3.4 *Calculations using independent, unconstrained models for high fluence*

Figure 15 shows calculated temperatures, diameters, and LII signals from the independent, unconstrained models for a fluence of 0.7 J/cm^2. At this high fluence the models yield less of a spread in predicted temperatures and signals than for the lower fluence (Fig. 6). The range of calculated diameter change, however, is much larger at the higher fluence. These differences between comparisons at low and high fluences are predominantly attributable to modeled sublimation rates. The Bladh and Hadef models predict an initial small increase in diameter, which is attributable to the decrease in density with temperature. Although the Michelsen model accounts for the temperature-dependent change in particle density, this effect is overwhelmed by the rapid loss of particle mass by photodesorption at this fluence. As at the lower fluence, $\dot{Q}_{\text{Absorption}}$ (Fig. 16a) has an influence on the maximum temperatures reached, but sublimation tends to limit peak temperatures, reducing the variability in predicted temperatures and hence signals. The variability in $\dot{Q}_{\text{Sublimation}}$ between the different models (Fig. 16b), however, leads to a range of calculated mass loss and size change.

Figure 17a shows the nearly linear dependence of $\dot{Q}_{\text{Absorption}}$ on $E(m)$. The Michelsen model shows an exception to this trend similar to that demonstrated at low fluence (Fig. 8a). The reason for the unusually high value for the Michelsen model is related to the nonlinear absorption that leads to photodesorption of C_2. The deviation of the Dreier model from the trend is currently not understood. The predicted peak temperature is not as strongly dependent on $E(m)$ as for the low-fluence case (Fig. 17b compared to Fig. 8b). The maximum signal is similarly not as strongly controlled by the peak temperature (Fig. 18 compared to Fig. 9). The large variability in the relationships between $E(m)$, peak temperature, and peak signal from the different models is attributable to differences in the way mass and heat loss by sublimation (and photodesorption) are handled.

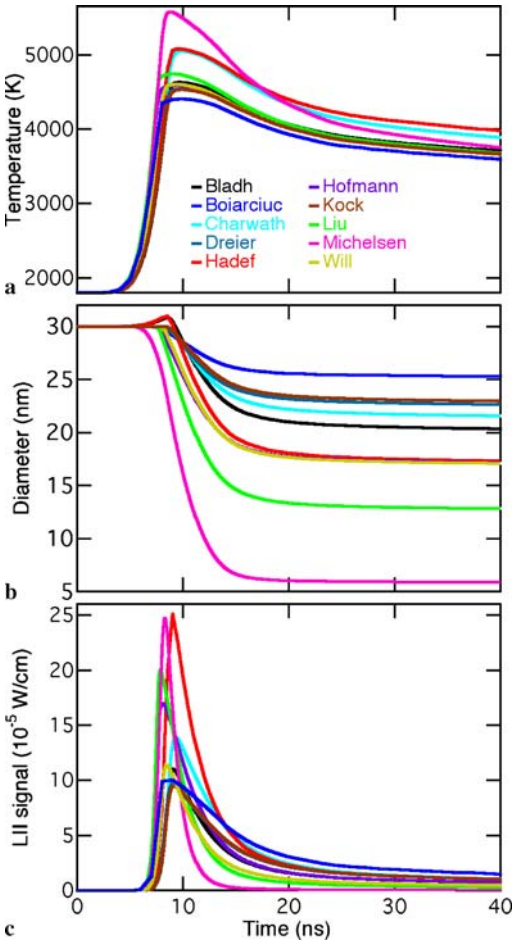

FIGURE 15 Comparison of modeled temperature, diameter, and LII signal from the unconstrained, independent models. Calculated (**a**) temperatures, (**b**) diameters, and (**c**) LII signals are shown as a function of time for ten models identified in the legend. Calculations were performed for a fluence of 0.70 J/cm^2

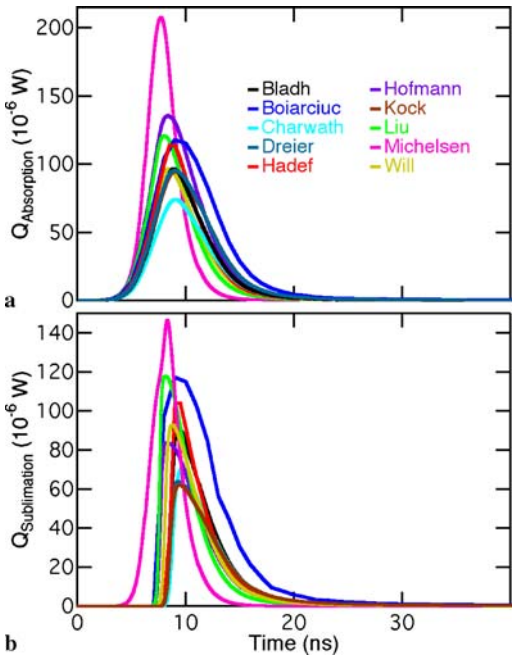

FIGURE 16 Comparison of absorptive-heating and evaporative-cooling rates from the unconstrained, independent models. Calculated values of (**a**) the absorptive-heating rate and (**b**) the evaporative-cooling rate are shown as a function of time for ten models identified in the legend. Calculations were performed for a fluence of 0.70 J/cm^2

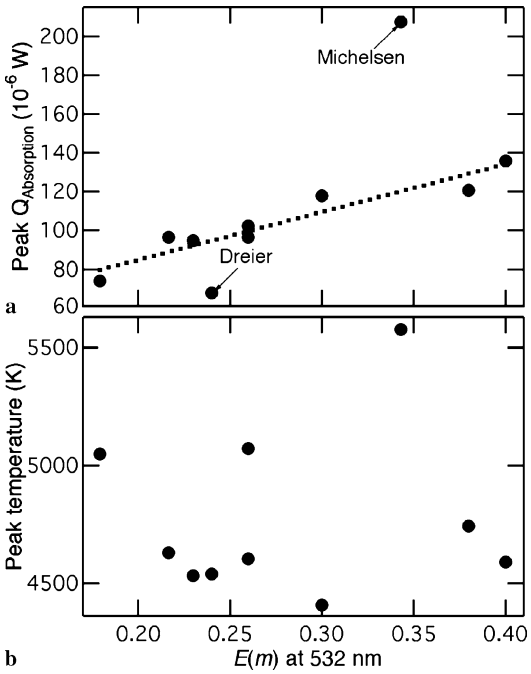

FIGURE 17 Dependence of the absorptive-heating rate and temperature on $E(m)$. The maxima of the (**a**) absorptive-heating rate curves (Fig. 16a) and (**b**) calculated temperature curves (Fig. 15a) are shown as a function of the value of $E(m)$ used in the unconstrained, independent models. Values that deviate from the linear correlation in (**a**) represented by the *dotted line* are identified by model. Calculations were performed for a fluence of 0.70 J/cm^2

Sublimation and particle-size change also have a strong influence on $\dot{Q}_{\text{Conduction}}$. Figure 19a shows a wide distribution in the magnitude and decay rate of the conductive-cooling rates. The conductive-cooling rate in the Michelsen model, for instance, decays much faster than in the other models; this behavior can be traced to the large particle-size change (Fig. 15b), which results from mass loss by photodesorption and sublimation. The decay rates of $\dot{Q}_{\text{Radiation}}$ (Fig. 19b) are similarly influenced by sublimation, photodesorption, and particle-size change.

Similarly to the low-fluence case, $\dot{Q}_{\text{Oxidation}}$ is approximately an order of magnitude smaller than $\dot{Q}_{\text{Conduction}}$ in the Michelsen model for the partial pressure of oxygen assumed, and oxidation has a negligible effect on the calculated signals. At the high fluence, however, $\dot{Q}_{\text{Thermionic}}$ is two orders of magnitude greater than $\dot{Q}_{\text{Conduction}}$ and is smaller than $\dot{Q}_{\text{Sublimation}}$ by less than a factor of 10. Thermionic emission reduces the calculated signal by $\sim 9\%$ at this fluence.

3.5 *Calculations using independent, constrained models for high fluence*

Constraining parameters for the high-fluence case significantly reduces differences in calculated temperatures, diameters, and signals between the models (Fig. 20 compared to Fig. 15). The most significant change in the agreement between the models is in the particle-size reduction (Fig. 20b). This change is probably attributable to better agreement in values of $\dot{Q}_{\text{Absorption}}$ (Fig. 21a compared to Fig. 16a), peak

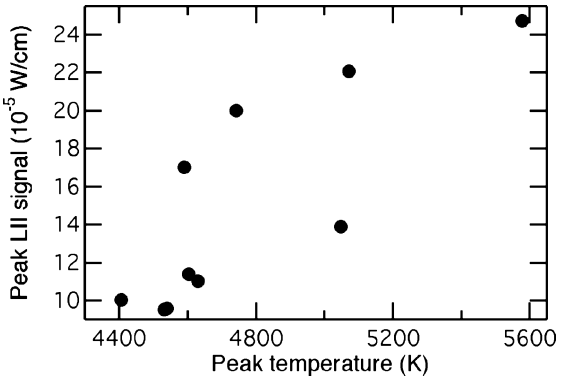

FIGURE 18 Dependence of the LII signal on temperature. The maxima of the calculated signal curves (Fig. 15c) are shown as a function of the maxima of the calculated temperature curves (Fig. 15a) for the unconstrained, independent models. Calculations were performed for a fluence of 0.70 J/cm^2

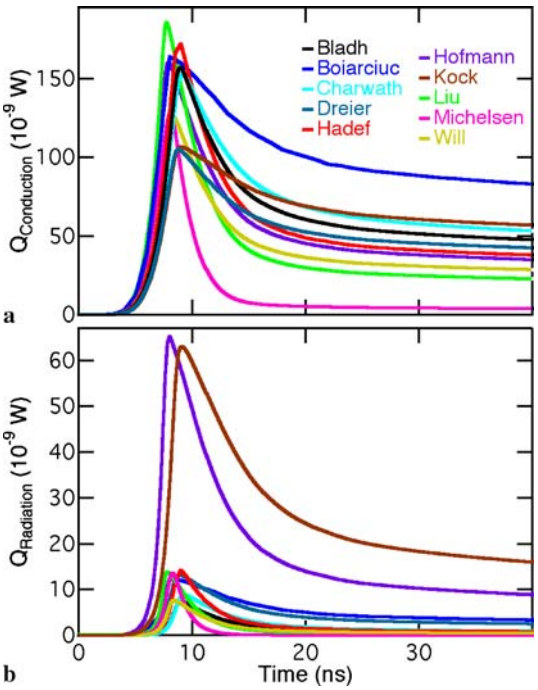

FIGURE 19 Comparison of conductive- and radiative-cooling rates from the unconstrained, independent models. Calculated values of (**a**) the conductive-cooling rate and (**b**) the radiative-cooling rate are shown as a function of time for ten models identified in the legend. Calculations were performed for a fluence of 0.70 J/cm^2

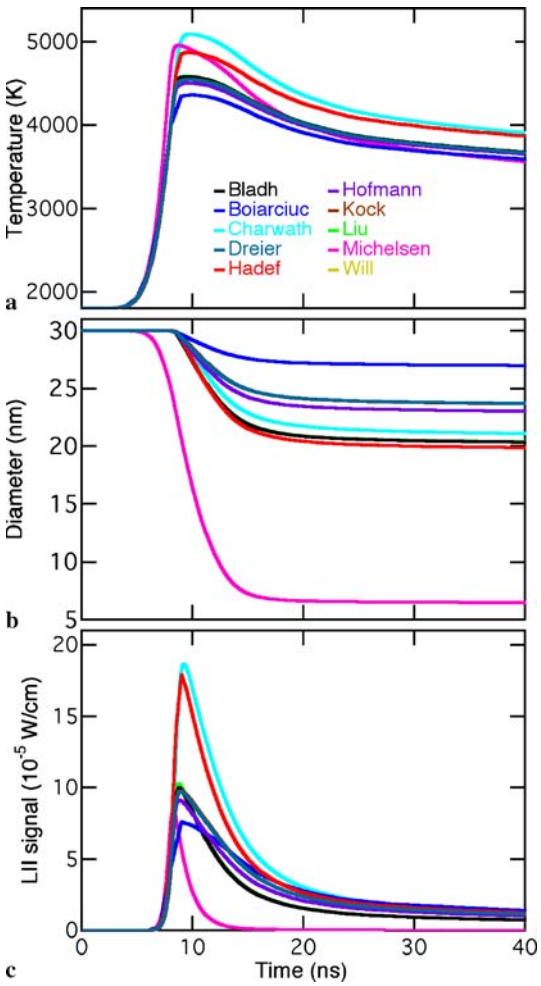

FIGURE 20 Comparison of modeled temperature, diameter, and LII signal from the constrained, independent models. Calculated (**a**) temperatures, (**b**) diameters, and (**c**) LII signals are shown as a function of time for ten models identified in the legend. Calculations were performed for a fluence of 0.70 J/cm^2

temperatures (Fig. 20a compared to Fig. 15a), and $\dot{Q}_{\text{Sublimation}}$ (Fig. 21b compared to Fig. 16b) because of constraints on $E(m)$ and α_{M}. The particle-size evolution is not substantially influenced by these constraints in the Michelsen model; the size change is predominantly attributable to the photodesorption of C_2, which is unchanged by the constraints on these parameters.

Although the spread in temperature and signal is reduced by constraining parameters, it is not as significantly reduced as in the low-fluence case, which is consistent with the larger scatter in the correlation of the peak temperature with $E(m)$ shown in Fig. 17b and in the correlation of the peak signal with temperature shown in Fig. 18.

Figure 22 shows the influence of constraining parameters on $\dot{Q}_{\text{Conduction}}$ and $\dot{Q}_{\text{Radiation}}$. The decay rates for these terms are still substantially larger in the Michelsen model than in the other models because of the much larger change in particle size caused by C_2 photodesorption. As in the low-fluence case the biggest differences between the models for the radiative-cooling rate are caused by the approach used to calculate $\dot{Q}_{\text{Radiation}}$. The range of values of the broadband $E(m)$ has less of an effect for this comparison.

4 Summary and conclusions

In the first organized LII model comparison [42, 43], modeled LII signals differed by so many orders of magnitude that they could not be compared without rescaling. The goal of the present study was to define the conditions well enough to perform a systematic comparison of model output and to determine magnitudes and identify sources of differences between models. The initial trial calculations used a fully constrained model based on the Melton model [16] and model parameters with defined input laser profile, particle size, and ambient conditions. These calculations allowed convergence of approaches for solving the energy- and mass-balance equations. The results

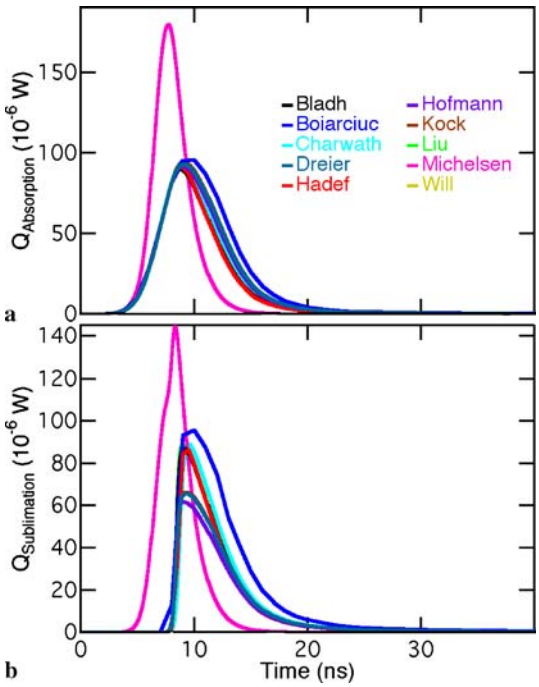

FIGURE 21 Comparison of absorptive-heating and evaporative-cooling rates from the constrained, independent models. Calculated values of (**a**) the absorptive-heating rate and (**b**) the evaporative-cooling rate are shown as a function of time for ten models identified in the legend. Calculations were performed for a fluence of $0.70\,\mathrm{J/cm^2}$

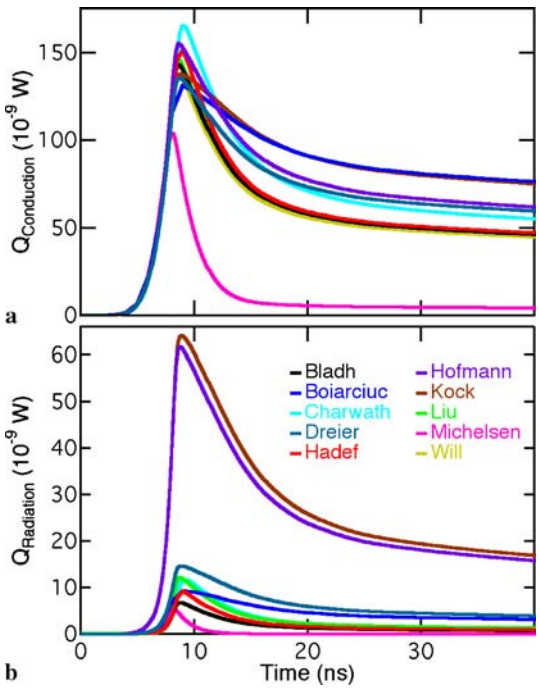

FIGURE 22 Comparison of conductive- and radiative-cooling rates from the constrained, independent models. Calculated values of (**a**) the conductive-cooling rate and (**b**) the radiative-cooling rate are shown as a function of time for ten models identified in the legend. Calculations were performed for a fluence of $0.70\,\mathrm{J/cm^2}$

from the fully constrained model calculations demonstrate small differences (up to 3.5% but generally $< 1\%$) resulting from equation-solving methodology and/or temporal resolution.

Ten independent models were used to perform calculations at low ($0.05\,\mathrm{J/cm^2}$) and high ($0.70\,\mathrm{J/cm^2}$) fluences. These comparisons demonstrate a large spread in model-predicted temperatures, diameters, and LII signals when the model parameters are unconstrained. This spread is significantly reduced when the models are run with constrained parameters. The analysis suggests that at low fluence the large differences between models are predominantly attributable to differences in values of $E(m)$ and α_T. At high fluence sublimation rates strongly influence calculated temperatures, diameters, and signals, in which case α_M may also contribute to variability. Constraining all of these parameters for the high-fluence case, however, does not decrease the variability in calculated temperatures and signals as significantly as it does for the low-fluence case. The high-fluence results appear to be sensitive to differences in the approach to calculating sublimation rates in addition to the parameters used.

The Michelsen model is the only model in the study that includes energy and mass loss by direct photodesorption of C_2 from the particle, heating and mass loss through oxidation by O_2, and energy loss to thermionic emission. The addition of photodesorption to the model has a very large effect on calculated temperatures, diameters, and signals at high fluence. For the partial pressure of oxygen assumed, oxidation has little effect on the model results. Thermionic emission has a negligible effect at low fluence but reduces the calculated signals by $\sim 9\%$ at high fluence.

5 Future directions

This study has been very useful for characterizing the magnitude of differences between LII models under the same input conditions and identifying the major sources of these differences under this limited set of input conditions. Future model comparisons could include testing the sensitivity of the models to input parameters, such as the primary particle size, excitation wavelength, ambient temperature and pressure, and aggregate morphology and size. Understanding the fluence dependence of the models would also be a useful goal.

In general the results of the comparisons presented here have shown that the LII models are very sensitive to selected parameters, which tend to have large uncertainties. More emphasis should be placed on narrowing the uncertainties in these parameters. Such a task could involve several approaches including

1. forming an advisory group to review the literature and compile a set of recommended values for experimentally measured parameters, e.g. ϱ_s, c_s, $E(m)$, α_T, and α_M and
2. measuring parameters that need to be known to better accuracy, e.g. temperature- and wavelength-dependent optical properties of soot, temperature-dependent thermal accommodation coefficients in different gases, and mass accommodation coefficients for carbon clusters on particle surfaces.

In addition, models should be validated with comparisons to a wide range of data obtained from detailed and well-controlled LII experiments, which will aid in identifying the best approaches and model parameters for modeling LII. Such validation studies would aid in a critique of the different phys-

ical formulations and parameters used in these LII models. As noted in the last model comparison [42, 43], experimental observations that would aid in model validation include

1. LII data recorded at low gas temperatures,
2. LII data recorded at high pressures,
3. LII data recorded at different laser wavelengths,
4. spectrally and temporally resolved emission data,
5. LII temporal profiles recorded with higher time resolution,
6. LII temporal profiles recorded over a wide range of fluences, and
7. single-particle LII data.

These data need to be recorded with smooth, well-defined spatial and temporal profiles.

Summary of parameters

B_j	parameter representing the influence of diffusive and convective mass and heat transfer during sublimation (bar) [36]
$B_{\lambda 1}$	empirically determined saturation coefficient for linear absorption ($0.6\,\mathrm{J/cm^2}$)
$B_{\lambda n}$	empirically determined saturation coefficient for multiphoton absorption ($0.5\,\mathrm{J/cm^2}$)
c	speed of light (2.998×10^{10} cm/s)
C_P^CO	molar heat capacity of CO (J/mol K) [36]
C_p	molar heat capacity of N_2 ($\sim$ air) at constant pressure (J/mol K) (Table 4)
c_s	specific heat of solid carbon (graphite) (J/g K) (Table 1, Fig. 3a)
C_v	molar heat capacity of N_2 ($\sim$ air) at constant volume (J/mol K)
D	primary particle diameter (cm)
D_0	initial primary particle diameter (30×10^{-7} cm, i.e. 30 nm, for this comparison)
$E(m)$	dimensionless refractive-index function (Table 2)
F	laser fluence ($\mathrm{J/cm^2}$); either $0.05\,\mathrm{J/cm^2}$ or $0.70\,\mathrm{J/cm^2}$ for this comparison
f	dimensionless Eucken correction to the thermal conductivity of a polyatomic gas
f_1	empirical scaling factor for linear absorption (1.2)
G	dimensionless geometry-dependent heat-transfer factor
h	Planck constant (6.626×10^{-34} J s)
K	dimensionless exponent used to define flux of sublimed clusters away from the surface (either 0.4 or 0.5)
k_B	Boltzmann constant (1.381×10^{-23} J/K)
k_ox	overall rate constant for oxidation ($1/\,\mathrm{s\,cm^2}$) [36]
k_p	Boltzmann constant in effective pressure units ($1.38065 \times 10^{-22}\,\mathrm{bar\,cm^3/K}$)
$k_{\lambda n}$	rate constant for removal of C_2 by photodesorption ($\mathrm{s^{-1}}$)
L	mean free path ($2.355 \times 10^{-8} T_0$ cm for the Melton model [16])
M	particle mass (g)
m_e	electron mass ($9.1095 \times 10^{-35}\,\mathrm{J\,s^2/cm^2}$)
n	estimated number of 532-nm photons absorbed to photodesorb C_2 (2)
N_A	Avogadro constant ($6.02214 \times 10^{23}\,\mathrm{mol^{-1}}$)
N_ss	density of carbon atoms on the surface of the particle ($2.8 \times 10^{15}\,\mathrm{cm^{-2}}$)
p_0	ambient pressure (1 bar = 0.98692 atm)
p_v	average partial pressure of sublimed carbon species (bar) (Table 3)
$p_\mathrm{v}^{C_j}$	thermal equilibrium partial pressure of sublimed C_j (bar) (Table 3)
p_ref	reference pressure used in Antoine and Clausius–Clapeyron equations (Table 3)
$p_\mathrm{sat}^{C_j}$	saturation partial pressure of C_j (bar)
$p_{\lambda n}$	effective pressure calculated from the rate of photodesorption of C_2 (bar)
q_1	normalization constant for the integrated laser temporal profile (7.79527×10^{-9} s for the laser profile provided)
q_n	normalization constant for the integrated laser temporal profile raised to the nth power (s)
$q(t)$	reduced laser temporal profile, unity at peak (unitless) (Fig. 2)
$\dot{Q}_\mathrm{Absorption}$	rate of energy gained by laser absorption (W)
$\dot{Q}_\mathrm{Conduction}$	rate of energy lost by conduction to the surrounding gases (W)
$\dot{Q}_\mathrm{Oxidation}$	rate of energy gained by oxidation of the particle (W)
$\dot{Q}_\mathrm{Radiation}$	rate of energy lost by radiative emission (W)
Q_Reduced	see (44) (unitless)
$\dot{Q}_\mathrm{Sublimation}$	rate of energy lost by sublimation and photodesorption of carbon clusters (W)
$\dot{Q}_\mathrm{Thermionic}$	rate of energy lost by thermionic emission (W)
R	universal gas constant (8.3145 J/mol K)
R_m	universal gas constant in effective mass units ($8.3145 \times 10^7\,\mathrm{g\,cm^2/mol\,K\,s^2}$)
R_p	universal gas constant in effective pressure units ($83.145\,\mathrm{bar\,cm^3/mol\,K}$)
S	calculated LII signal (J/cm s for this comparison) at 500 nm over the entire particle surface
t	time (s)
T	particle temperature (K)
T_δ	temperature in the boundary layer of the particle (K) [40]
T_ref	reference temperature used in Clausius–Clapeyron equation (K) (Table 3)
T_0	initial particle temperature and temperature of the surrounding gas, assumed to be 1800 K for this comparison
U_j	mean velocity of C_j away from the particle surface assuming a Maxwell speed distribution at the surface temperature (cm/s)
U_Internal	internal energy of the particle (J)
W_a	average molecular weight of air (28.74 g/mol)
W_j	molecular weight of species C_j ($j \times 12.011$ g/mol)
W_v	average molecular weight of sublimed carbon species (g/mol) (Table 3)
α_j	mass accommodation coefficient of vaporized species C_j (Table 3)
α_M	species-independent mass accommodation coefficient of vaporized carbon clusters (Table 3)

α_T thermal accommodation coefficient of ambient gases with the surface (Table 4)
β scaling factor for emissivity ($28.72\,\mathrm{cm}^{-0.17}$)
γ heat-capacity ratio (C_p/C_V) for the gas surrounding the particles (Table 4, Fig. 3c)
γ^* average heat-capacity ratio (C_p/C_V) for the gas surrounding the particles
ΔH_j enthalpy of formation of carbon vapor species C_j (J/mol) (Table 3)
ΔH_v average enthalpy of formation of sublimed carbon species C_j (J/mol) (Table 3)
ΔH_{ox} enthalpy of reaction for $2C + O_2 \rightarrow 2CO$ (-2.215×10^5 J/mol)
$\Delta H_{\lambda n}$ energy required to photodesorb C_2 (3.4×10^5 J/mol)
ε_λ emissivity at wavelength λ
κ_a thermal conductivity of ambient gas ($5.83 \times 10^{-5}\,(T/273)^{0.82}$ W/cm K for the original Melton model [16]; 1×10^{-3} W/cm K for the comparison runs of the Melton model; 1.068×10^{-3} W/cm K for the Will model; $1.0811 \times 10^{-4} + 5.1519 \times 10^{-7}\,T$ W/cm K for the Bladh model [36])
λ laser wavelength (532 nm for this comparison)
λ_s emission wavelength for signal calculation (500 nm for this comparison)
ξ dispersion exponent (0.83)
ϱ_s density of graphite (Table 1, Fig. 3b)
$\bar{\sigma}$ average molecular cross section for subliming species
σ average molecular cross section for air ($\sim 3.0 \times 10^{-15}\,\mathrm{cm}^2$ at 1800 K)
σ_{SB} Stefan–Boltzmann constant (5.6704×10^{-12} W/cm^{2}K^4)
$\sigma_{\lambda n}$ empirically determined multiphoton absorption cross section for photodesorption of C_2 ($1.9 \times 10^{-10}\,\mathrm{cm}^{2n-1}\mathrm{J}^{1-n}$)
ϕ work function (7.37×10^{-19} J)

ACKNOWLEDGEMENTS Funding for the 2006 LII workshop in Bad Herrenalb, Germany was provided by the Deutsche Forschungsgemeinschaft (DFG), Coherent, InnoLas, La Vision, PCO, Quantel, and Radiant Dyes Laser. H. Bladh and P.-E. Bengtsson thank the Swedish Research Council for support and the European Commission for its financial contribution to this work within the AEROTEST project, Contract No. AST3-CT-2004-502856, Auxitrol S.A. H. Bockhorn, M. Charwath, M. Hofmann, B.F. Kock, C. Schulz, R. Suntz, and B. Tribalet were supported by the DFG. T. Dreier acknowledges the financial support of the Swiss Federal Office of Energy (BFE) and the Swiss National Fund (SNF). R. Hadef thanks the Alexander von Humboldt Stiftung for the award of a fellowship to carry out this research. H.A. Michelsen was funded by the Division of Chemical Sciences, Geosciences, and Biosciences, the Office of Basic Energy Sciences, the US Department of Energy. Sandia is a multi-program laboratory operated by Sandia Corporation, a Lockheed Martin Company, for the National Nuclear Security Administration under Contract No. DE-AC04-94-AL85000.

REFERENCES

1 J.E. Dec, SAE Paper 920115 (1992)
2 J.E. Dec, A.O. zur Loye, D.L. Siebers, SAE Paper 910224 (1991)
3 C. Espey, J.E. Dec, SAE Paper 930971 (1993)
4 N.P. Tait, D.A. Greenhalgh, Ber. Bunsenges. Phys. Chem. **97**, 1619 (1993)
5 R.L. Vander Wal, D.L. Dietrich, Appl. Opt. **34**, 1103 (1995)
6 R.L. Vander Wal, K.J. Weiland, Appl. Phys. B **59**, 445 (1994)
7 C. Crua, D.A. Kennaird, M.R. Heikal, Combust. Flame **135**, 475 (2003)
8 M.D. Smooke, M.B. Long, B.C. Connelly, M.B. Colket, R.J. Hall, Combust. Flame **143**, 613 (2005)
9 C. Schoemaecker Moreau, E. Therssen, X. Mercier, J.F. Pauwels, P. Desgroux, Appl. Phys. B **78**, 485 (2004)
10 T. Schittkowski, B. Mewes, D. Brüggemann, Phys. Chem. Chem. Phys. **4**, 2063 (2002)
11 T. Ni, J.A. Pinson, S. Gupta, R.J. Santoro, Appl. Opt. **34**, 7083 (1995)
12 C.R. Shaddix, K.C. Smyth, Combust. Flame **107**, 418 (1996)
13 A. Boiarciuc, F. Foucher, C. Mounaïm-Rousselle, Appl. Phys. B **83**, 413 (2006)
14 A.C. Eckbreth, J. Appl. Phys. **48**, 4473 (1977)
15 R.W. Weeks, W.W. Duley, J. Appl. Phys. **45**, 4661 (1974)
16 L.A. Melton, Appl. Opt. **23**, 2201 (1984)
17 C.J. Dasch, Appl. Opt. **23**, 2209 (1984)
18 D.L. Hofeldt, SAE Paper 930079 (1993)
19 S. Will, S. Schraml, A. Leipertz, Opt. Lett. **20**, 2342 (1995)
20 S. Will, S. Schraml, K. Bader, A. Leipertz, Appl. Opt. **37**, 5647 (1998)
21 B. Mewes, J.M. Seitzman, Appl. Opt. **36**, 709 (1997)
22 P. Roth, A.V. Filippov, J. Aerosol Sci. **27**, 95 (1996)
23 A.V. Filippov, M.W. Markus, P. Roth, J. Aerosol Sci. **30**, 71 (1999)
24 S. Schraml, S. Dankers, K. Bader, S. Will, A. Leipertz, Combust. Flame **120**, 439 (2000)
25 C. Allouis, F. Rosano, F. Beretta, A. D'Alessio, Meas. Sci. Technol. **13**, 401 (2002)
26 T. Lehre, B. Jungfleisch, R. Suntz, H. Bockhorn, Appl. Opt. **42**, 2021 (2003)
27 T. Lehre, H. Bockhorn, B. Jungfleisch, R. Suntz, Chemosphere **51**, 1055 (2003)
28 B.F. Kock, T. Eckhardt, P. Roth, Proc. Combust. Inst. **29**, 2775 (2002)
29 B.F. Kock, C. Kayan, J. Knipping, H.R. Orthner, P. Roth, Proc. Combust. Inst. **30**, 1689 (2005)
30 B.F. Kock, B. Tribalet, C. Schulz, P. Roth, Combust. Flame **147**, 79 (2006)
31 V. Krüger, C. Wahl, R. Hadef, K.P. Geigle, W. Stricker, M. Aigner, Meas. Sci. Technol. **16**, 1477 (2005)
32 J. Appel, B. Jungfleisch, M. Marquardt, R. Suntz, H. Bockhorn, Proc. Combust. Inst. **26**, 2387 (1996)
33 K.R. McManus, J.H. Frank, M.G. Allen, W.T. Rawlins, Proc. AIAA **36**, 98 (1998)
34 D. Snelling, F. Liu, G.J. Smallwood, Ö.L. Gülder, in *Proc. 34th Natl. Heat Transfer Conf. (NHTC2000-12132)*, Pittsburgh, Pennsylvania, USA, 2000
35 G.J. Smallwood, D. Snelling, F. Liu, Ö.L. Gülder, J. Heat Transfer **123**, 814 (2001)
36 H.A. Michelsen, J. Chem. Phys. **118**, 7012 (2003)
37 H. Bladh, P.-E. Bengtsson, Appl. Phys. B **78**, 241 (2004)
38 D.R. Snelling, F. Liu, G.J. Smallwood, Ö.L. Gülder, Combust. Flame **136**, 180 (2004)
39 F. Liu, K.J. Daun, D.R. Snelling, G.J. Smallwood, Appl. Phys. B **83**, 355 (2006)
40 F. Liu, M. Yang, F.A. Hill, D.R. Snelling, G.J. Smallwood, Appl. Phys. B **83**, 383 (2006)
41 V. Beyer, D.A. Greenhalgh, Appl. Phys. B **83**, 455 (2006)
42 C. Schulz, B.F. Kock, M. Hofmann, H.A. Michelsen, S. Will, B. Bougie, R. Suntz, G.J. Smallwood, Appl. Phys. B **83**, 333 (2006)
43 http://www.vug.uni-duisburg.de/IVG/index.html
44 http://www.vbt.uni-karlsruhe.de/specialtopic/2ndLIIWS2006/Internetauftritt1.htm
45 B.J. McCoy, C.Y. Cha, Chem. Eng. Sci. **29**, 381 (1974)
46 M.W. Chase Jr., J. Phys. Chem. Ref. Data Monogr. 9 **14**, 535 (1998)
47 L.E. Fried, W.M. Howard, Phys. Rev. B **61**, 8734 (1999)
48 C.F. Bohren, D.R. Huffman, *Absorption and Scattering of Light by Small Particles* (Wiley, New York, 1983)
49 Ü.Ö. Köylü, Combust. Flame **109**, 488 (1996)
50 Ü.Ö. Köylü, G.M. Faeth, J. Heat Transfer **118**, 415 (1996)
51 H.R. Leider, O.H. Krikorian, D.A. Young, Carbon **11**, 555 (1973)
52 E.R.G. Eckert, R.M. Drake Jr., *Analysis of Heat and Mass Transfer* (McGraw-Hill, New York, 1972)
53 W.M. Rohsenow, H.Y. Choi, *Heat, Mass, and Momentum Transfer* (Prentice-Hall, Englewood Cliffs, NJ, 1961)
54 A.V. Filippov, D.E. Rosner, Int. J. Heat Mass Transf. **43**, 127 (2000)
55 C. Kittel, *Introduction to Solid State Physics*, 6th edn. (Wiley, New York, 1986)

56 S.C. Graham, J.B. Homer, J.L.J. Rosenfeld, Proc. R. Soc. London A **344**, 259 (1975)
57 Degussa AG, Pigmentruße/Pigment Blacks, Technische Daten/Technical Data, Frankfurt
58 W.H. Dalzell, A.F. Sarofim, J. Heat Transf. **91**, 100 (1969)
59 K.C. Smyth, C.R. Shaddix, Combust. Flame **107**, 314 (1996)
60 H. Chang, T.T. Charalampopoulos, Proc. R. Soc. London A **430**, 577 (1990)
61 S.S. Krishnan, K.-C. Lin, G.M. Faeth, J. Heat Transf. **123**, 331 (2001)
62 M.P. Hoffman, F.A. Rigby, AIAA J. **29**, 927 (1991)
63 L. Brewer, J.S. Kane, J. Phys. Chem. **59**, 105 (1955)
64 Landolt-Börnstein, *Zahlenwerte und Funktionen aus Naturewissenschaften und Technik*, vol. II/2a, 6th edn. (Springer, Berlin, 1960)
65 J. Häger, D. Glatzer, H. Kuze, M. Fink, H. Walther, Surf. Sci. **374**, 181 (1997)
66 O. Leroy, J. Perrin, J. Jolly, M. Péalat, M. Lefebvre, J. Phys. D **30**, 499 (1997)
67 S.C. Saxena, R.K. Joshi, *Thermal Accommodation and Absorption Coefficients of Gases* (McGraw-Hill, New York, 1981)
68 S.-A. Kuhlmann, J. Reimann, S. Will, J. Aerosol Sci. **37**, 1696 (2006)